



Two-dimensional stability analysis of finite-amplitude interfacial gravity waves in a two-layer fluid

Sunao Murashige¹,† and Wooyoung Choi²

(Received 10 August 2021; revised 9 December 2021; accepted 14 February 2022)

We explore basic mechanisms for the instability of finite-amplitude interfacial gravity waves through a two-dimensional linear stability analysis of the periodic and irrotational plane motion of the interface between two unbounded homogeneous fluids of different density in the absence of background currents. The flow domains are conformally mapped into two half-planes, where the time-varying interface is always mapped onto the real axis. This unsteady conformal mapping technique with a suitable representation of the interface reduces the linear stability problem to a generalized eigenvalue problem, and allows us to accurately compute the growth rates of unstable disturbances superimposed on steady waves for a wide range of parameters. Numerical results show that the wave-induced Kelvin-Helmholtz (KH) instability due to the tangential velocity jump across the interface produced by the steady waves is the major instability mechanism. Any disturbances whose dominant wavenumbers are greater than a critical value grow exponentially. This critical wavenumber that depends on the steady wave steepness and the density ratio can be approximated by a local KH stability analysis, where the spatial variation of the wave-induced currents is neglected. It is shown, however, that the growth rates need to be found numerically with care and the successive collisions of eigenvalues result in the wave-induced KH instability. In addition, the present study extends the previous results for the small-wavenumber instability, such as modulational instability, of relatively small-amplitude steady waves to finite-amplitude ones.

Key words: internal waves

¹Department of Mathematics and Informatics, Ibaraki University, Mito, Ibaraki 310-8512, Japan

²Department of Mathematical Sciences, New Jersey Institute of Technology, Newark, NJ 07102-1982, USA

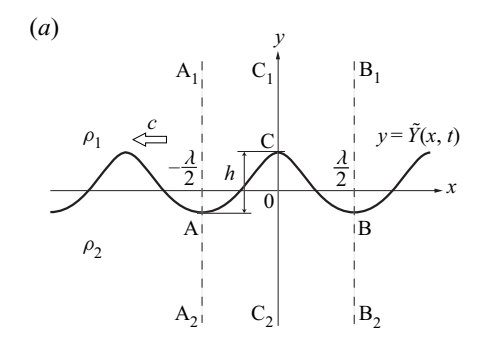
1. Introduction

Progressive gravity waves at the interface between two homogenous fluids of different density have been extensively studied as a simple model for internal waves which are commonly observed on a pycnocline in the ocean. This work numerically considers the two-dimensional linear stability of the periodic and irrotational plane motion of steady interfacial gravity waves propagating in permanent form with constant speed at the interface between two unbounded homogeneous fluids in the absence of background currents, as shown in figure 1(a). The fluids are assumed to be incompressible and inviscid, the surface tension at the interface is neglected and the density of the upper-layer fluid (ρ_1) is assumed to be less than that of the lower-layer fluid (ρ_2) for static stability.

For finite-amplitude steady interfacial waves, the full Euler system has been numerically studied by Holyer (1979), Vanden-Broeck (1980), Saffman & Yuen (1982), Meiron & Saffman (1983), Turner & Vanden-Broeck (1986) and Părău & Dias (2001). In particular, Saffman & Yuen (1982) developed a numerical method to find steady wave solutions in the hodograph plane, which can be recovered, in the steady limit, from our unsteady formulation to be presented. It should be remarked that, unlike surface gravity waves, the wave profiles of large-amplitude steady interfacial waves of permanent form may overhang, as shown in Meiron & Saffman (1983) and Turner & Vanden-Broeck (1986). However, the limiting behaviour of steady interfacial waves is not yet known. On the other hand, adopting the Stokes expansion in small wave steepness, Tsuji & Nagata (1973) obtained the fifth-order approximate steady wave solutions, which we compare with our fully nonlinear numerical solutions for steady waves.

The linear stability of steady interfacial periodic waves has been investigated by Yuen (1984), Grimshaw & Pullin (1985), Pullin & Grimshaw (1985), Dixon (1990) and Zhou, Lee & Cheung (1992). In their earlier attempts, Yuen (1984) and Pullin & Grimshaw (1985) numerically solved the linear stability problem in the physical plane using the method that McLean (1982) developed for the stability analysis of surface waves. With k and h denoting the wavenumber and the crest-to-trough wave height of the steady waves, respectively, Yuen (1984) obtained the numerical results for two different wave steepnesses, kh = 0.2 and 0.5, for density ratios of $\rho_1/\rho_2 = 0.1$ and 0.9, but the numbers of Fourier modes for the computation of steady waves and for the stability analysis were 20 and 5, respectively, which are too small for accurate computations. On the other hand, Pullin & Grimshaw (1985) presented results for greater wave steepnesses $kh \leq 0.3\pi$ ($\simeq 0.942$) under the Boussinesq approximation for the density ratio $\rho_1/\rho_2 \rightarrow 1$, where the density difference across the interface is ignored except for the buoyancy term. Their results showed that the instabilities due to low-order resonances, including the modulational instability of small- and moderate-steepness waves, are analogous to those for surface waves (McLean 1982). Dixon (1990) and Zhou et al. (1992) obtained similar results using the Zakharov formulation for interfacial waves. As they focused on the modulational instability for small-steepness waves perturbed by small-wavenumber disturbances, Grimshaw & Pullin (1985, (4.4) on p. 304) also derived a nonlinear Schrödinger equation as a weakly nonlinear model, whose solutions are compared with their numerical solutions.

In addition to the small-wavenumber or modulational instability, Pullin & Grimshaw (1985, figure 10 on p. 331) numerically found a large-wavenumber instability for $\rho_1/\rho_2 \rightarrow 1$ and $kh = 0.2\pi$ ($\simeq 0.628$), which is similar to the Kelvin–Helmholtz (KH) instability that usually occurs in the presence of a background current jump at the interface. This KH-type instability is excited by the tangential velocity jump induced by the steady wave at the interface. This instability has been referred to as the 'wave-induced KH instability' and



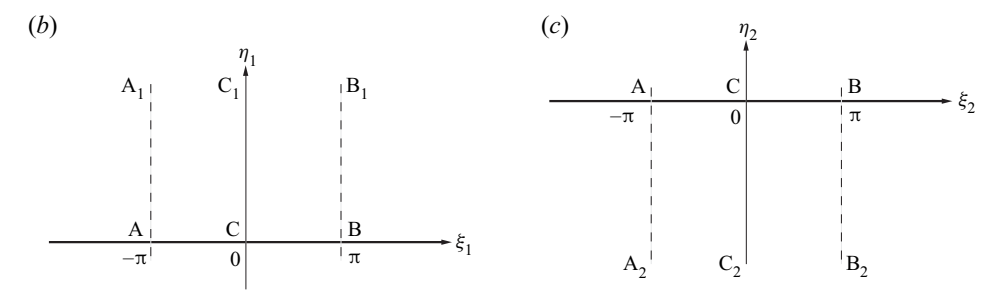


Figure 1. Two-dimensional periodic motion of interfacial waves and conformal mapping of the flow domains: (a) the z-plane (z = x + iy), (b) the ζ_1 -plane ($\zeta_1 = \xi_1 + i\eta_1$) and (c) the ζ_2 -plane ($\zeta_2 = \xi_2 + i\eta_2$). The upper- and lower-layer flow domains in the physical plane (the z-plane) are conformally mapped onto the upper half of the ζ_1 -plane and the lower half of the ζ_2 -plane, respectively. Here, h: the crest-to-trough wave height, λ : the wavelength and ρ_i (i = 1, 2): the fluid density of the jth layer.

does not occur for surface waves. Pullin & Grimshaw (1985, (4.1) on p. 330) proposed an approximate expression for the growth rate of the wave-induced KH instability using linear theory for the well-known KH instability for two horizontal uniform currents of different speed (for example, see Lamb (1945, § 232) and Drazin & Reid (1981, § 1.4)), and pointed out that this instability occurs if the wavenumber of a disturbance added to the steady wave is greater than a critical value. However, this instability was studied only for one value of the wave steepness, $kh = 0.2\pi$ ($\simeq 0.628$), under the Boussinesq approximation, and was not fully examined. Dixon (1990, § 6) also discussed this instability using the Zakharov formulation, but computed the growth rate only for a single wave steepness of kh = 0.4.

Although its growth rate is much greater than that of the modulational instability, the wave-induced KH instability has not been studied extensively and a more complete study is required to better understand the instability of interfacial gravity waves for a wide range of steady wave steepnesses. It is, however, difficult to numerically study this instability using the previous numerical methods developed in the physical plane, particularly, when the wave steepness is no longer small. Instead, the stability problem needs to be investigated by adopting a new technique relevant for the unsteady motion of large-amplitude waves.

In this work, the two flow domains in a two-layer fluid are conformally mapped into two half-planes, where the time-varying interface is always mapped onto the real axis in each plane, as shown in figure 1. This unsteady conformal mapping technique (Ovshannikov 1974; Tanveer 1991; Dyachenko, Zakharov & Kuznetsov 1996; Choi & Camassa 1999) has been successfully used for the two-dimensional linear instability analysis of surface capillary waves by Tiron & Choi (2012) and surface gravity waves on a linear shear current by Murashige & Choi (2020). The aim of this work is to numerically study various

instabilities of interfacial gravity waves including the wave-induced KH instability and the modulational instability through two-dimensional linear stability analysis using this unsteady conformal mapping technique.

The paper is organized as follows. The basic formulation for the two-layer problem using the unsteady conformal mapping is presented in § 2. Computed steady interfacial periodic waves with symmetric profiles are shown in § 3. The details of our linear stability analysis are described in § 4. In comparison with the theoretical approximations of the growth rates of unstable disturbances presented in § 5, our numerical results of the linear stability analysis are summarized and discussed in § 6. Section 7 concludes this work.

2. Formulation of the problem

2.1. Formulation in the physical plane

Consider the periodic and irrotational plane motion of steady gravity waves progressing to the left in permanent form with constant speed c at the interface between two unbounded homogeneous fluids with the different densities ρ_1 and ρ_2 ($\rho_1 < \rho_2$), as shown in figure 1(a), where subscripts 1 and 2 refer to the upper and lower fluid domains, respectively. It is convenient to formulate the problem in the flow domains for one period with wavelength λ of the steady waves, namely the two domains surrounded by A_jACBB_j (j=1,2) in figure 1(a), in the frame of reference moving to the left with the waves. The steady wave profiles are assumed to be symmetric with respect to the vertical line passing through the wave crest. It is also assumed that the fluids are incompressible and inviscid, and that the fluid motion in each layer is two-dimensional and irrotational in the vertical cross-section (x, y) along the propagation direction of the waves. Surface tension at the interface is neglected. The origin is placed such that the wave profile $y = \tilde{Y}(x, t)$ satisfies the zero mean level condition

$$\int_0^{\lambda} \tilde{Y}(x,t) \, \mathrm{d}x = 0, \tag{2.1}$$

where *t* denotes the time.

For irrotational plane flows, we can introduce the complex coordinate z = x + iy and the complex velocity potential $f_j = \phi_j + i\psi_j$ (j = 1, 2), where ϕ_j and ψ_j denote the velocity potential and the streamfunction, respectively, for the *j*th layer. When the physical variables are non-dimensionalized, with respect to c and k ($=2\pi/\lambda$), as

$$z_* = kz$$
, $\tilde{Y}_* = k\tilde{Y}$, $t_* = ckt$, $f_{j*} = \frac{f_j}{c/k}$, $p_{j*} = \frac{p_j}{\rho_1 c^2}$ $(j = 1, 2)$, (2.2)

the following dimensionless parameters appear in the problem:

$$h_* = kh, \quad c_* = \frac{c}{\sqrt{g/k}},$$
 (2.3)

where p_j denote the pressure, h the crest-to-trough wave height and g the gravitational acceleration. Note that $h_* = kh = 2\pi h/\lambda$ is the wave steepness. The asterisks for dimensionless variables will be omitted hereinafter for brevity.

The complex velocity potentials $f_j = f_j(z, t)$ (j = 1, 2) are both analytic in each layer. The boundary conditions at the interface $y = \tilde{Y}(x, t)$ are given, from the kinematic

conditions, by

$$\tilde{Y}_t + \phi_{j,x}\tilde{Y}_x = \phi_{j,y} \quad (j = 1, 2) \quad \text{at } y = \tilde{Y}(x, t),$$
 (2.4)

and, from the dynamic condition $p_1 = p_2$ at the interface $y = \tilde{Y}(x, t)$ with Bernoulli's equation for each layer, by

$$\phi_{1,t} + \frac{1}{2}(\phi_{1,x}^2 + \phi_{1,y}^2) + \frac{1}{c^2}\tilde{Y} - B(t)$$

$$= \frac{\rho_2}{\rho_1} \left\{ \phi_{2,t} + \frac{1}{2}(\phi_{2,x}^2 + \phi_{2,y}^2) + \frac{1}{c^2}\tilde{Y} \right\} \quad \text{at } y = \tilde{Y}(x,t), \tag{2.5}$$

where an arbitrary function B(t) can be absorbed into the velocity potentials and the subscripts denote the partial derivatives with respect to x, y and t as

$$\tilde{Y}_x := \frac{\partial \tilde{Y}}{\partial x}, \quad \tilde{Y}_t := \frac{\partial \tilde{Y}}{\partial t}, \quad \phi_{j,x} := \frac{\partial \phi_j}{\partial x}, \quad \phi_{j,y} := \frac{\partial \phi_j}{\partial y} \quad \text{and} \quad \phi_{j,t} := \frac{\partial \phi_j}{\partial t} \quad (j = 1, 2).$$
(2.6)

To avoid any confusion, a comma is introduced to denote a derivative of an indexed function with respect to the variable following the comma.

It should be remarked that, as a velocity jump across the interface is allowed under the inviscid assumption, the velocity potential is discontinuous across the interface while the streamfunction is continuous so that

$$\psi_1(x, y, t) = \psi_2(x, y, t)$$
 at $y = \tilde{Y}(x, t)$. (2.7)

In addition, the conditions that the flow is uniform far above and below the interface $(y \to \pm \infty)$ yield

$$w_1 := \frac{\partial f_1}{\partial z} \to 1 \quad \text{as } y \to \infty \quad \text{and} \quad w_2 := \frac{\partial f_2}{\partial z} \to 1 \quad \text{as } y \to -\infty,$$
 (2.8)

where $w_j = u_j - iv_j$ (j = 1, 2) denote the complex velocity.

2.2. Unsteady conformal mapping of the flow domains

As described in § 1, in order to overcome numerical difficulties for the two-dimensional linear stability analysis of finite-amplitude interfacial waves, we generalize the unsteady conformal mapping technique used for the stability of surface capillary and gravity waves (Tiron & Choi 2012; Murashige & Choi 2020) to the two-layer problem. Here, we map the upper flow domain $(y > \tilde{Y}(x,t))$ and the lower flow domain $(y < \tilde{Y}(x,t))$ into the upper half of the ζ_1 -plane $(\zeta_1 = \xi_1 + i\eta_1 \text{ with } \eta_1 > 0)$ and the lower half of the ζ_2 -plane $(\zeta_2 = \xi_2 + i\eta_2 \text{ with } \eta_2 < 0)$, respectively, as shown in figures 1(b) and 1(c). The time-varying interface $y = \tilde{Y}(x,t)$ is always mapped onto the real axes $\eta_j = 0$ in the ζ_j -plane (j = 1, 2) although the corresponding physical locations on the interface are different even when $\xi_1 = \xi_2$.

The complex coordinates $z_j = z(\zeta_j, t) = x_j(\xi_j, \eta_j, t) + iy_j(\xi_j, \eta_j, t)$ and the complex velocity potentials $f_j(\zeta_j, t) = \phi_j(\xi_j, \eta_j, t) + i\psi_j(\xi_j, \eta_j, t)$ are analytic in the ζ_j -plane (j = 1, 2). We write x_i, y_i, ϕ_i and ψ_i at the interface $\eta_i = 0$ (j = 1, 2) as

$$\tilde{x}_{j}(\xi_{j}, t) = x_{j}(\xi_{j}, \eta_{j} = 0, t), \quad \tilde{y}_{j}(\xi_{j}, t) = y_{j}(\xi_{j}, \eta_{j} = 0, t)
\tilde{\phi}_{j}(\xi_{j}, t) = \phi_{j}(\xi_{j}, \eta_{j} = 0, t), \quad \tilde{\psi}_{j}(\xi_{j}, t) = \psi_{j}(\xi_{j}, \eta_{j} = 0, t)
(j = 1, 2).$$
(2.9)

Note that, at the interface, ξ_j (j=1,2) range from $-\pi$ to π for one wavelength, as shown in figures 1(b) and 1(c). We also introduce the following shorthand notation for partial

derivatives with respect to ξ_i and t, respectively, as

$$x_{j,j} := \frac{\partial x_j}{\partial \xi_i}$$
 and $x_{j,t} := \frac{\partial x_j}{\partial t}$ $(j = 1, 2).$ (2.10)

Then, using the chain rule, it can be shown that the derivatives in the *z*-plane can be transformed to those in the ζ_j -plane (j = 1, 2) as

$$\phi_{j,x} = \frac{1}{J_j} \frac{\partial(\phi_j, y_j)}{\partial(\xi_j, \eta_j)}, \quad \phi_{j,y} = \frac{1}{J_j} \frac{\partial(x_j, \phi_j)}{\partial(\xi_j, \eta_j)}, \quad \phi_{j,t} = \frac{1}{J_j} \frac{\partial(x_j, y_j, \phi_j)}{\partial(\xi_j, \eta_j, t)} \quad (j = 1, 2), \quad (2.11)$$

$$\tilde{Y}_x = \frac{\tilde{y}_{j,j}}{\tilde{x}_{j,j}} \quad \text{and} \quad \tilde{Y}_t = \frac{1}{\tilde{x}_{j,j}} \frac{\partial (\tilde{x}_j, \tilde{y}_j)}{\partial (\xi_j, t)} \quad (j = 1, 2),$$
 (2.12)

where J_i (j = 1, 2) are defined by

$$J_i := x_{i,i}^2 + y_{i,i}^2 \quad (j = 1, 2).$$
 (2.13)

In order to match at the interface $\eta_j = 0$ (j = 1, 2) the upper- and lower-layer solutions, we introduce a subsidiary real variable $\hat{\xi}$ along the interface and write ξ_1 and ξ_2 at the interface as

$$\xi_1(\hat{\xi}, t) = \hat{\xi} + \gamma(\hat{\xi}, t)$$
 and $\xi_2(\hat{\xi}, t) = \hat{\xi} - \gamma(\hat{\xi}, t)$ for $-\pi \leqslant \hat{\xi} \leqslant \pi$, (2.14)

with

$$\xi_j(\hat{\xi} = \pm \pi, t) = \pm \pi \quad (j = 1, 2) \quad \text{and} \quad \gamma(\hat{\xi} = \pm \pi, t) = 0 \quad \text{for } t \ge 0,$$
 (2.15)

where $\gamma(\hat{\xi}, t)$ is an unknown real function. Note that similar parametric representations of the interface have been previously adopted for the numerical computation of steady interfacial waves (Saffman & Yuen 1982; Părău & Dias 2001) and unsteady interfacial waves (Baker, Meiron & Orszag 1982; Grue *et al.* 1997).

Using $\hat{\xi}$ and γ defined by (2.14), the conditions that the wave profiles in the ζ_1 - and ζ_2 -planes coincide are given by

$$\tilde{x}_{1}(\xi_{1} = \xi_{1}(\hat{\xi}, t), t) = \tilde{x}_{2}(\xi_{2} = \xi_{2}(\hat{\xi}, t), t)
\tilde{y}_{1}(\xi_{1} = \xi_{1}(\hat{\xi}, t), t) = \tilde{y}_{2}(\xi_{2} = \xi_{2}(\hat{\xi}, t), t)$$
(2.16)

The conditions in (2.16) are referred to as the contact conditions at the interface in this work. Also the continuity condition (2.7) of the streamfunctions at the interface can be expressed as

$$\tilde{\psi}_1(\xi_1 = \xi_1(\hat{\xi}, t), t) = \tilde{\psi}_2(\xi_2 = \xi_2(\hat{\xi}, t), t). \tag{2.17}$$

Substituting (2.11) and (2.12) with the Cauchy–Riemann relations into (2.4) and (2.5), we obtain the kinematic conditions and the dynamic condition at the interface $\eta_j = 0$ in the ξ_j -plane (j = 1, 2), respectively, as

$$\tilde{x}_{j,j}\tilde{y}_{j,t} - \tilde{y}_{j,j}\tilde{x}_{j,t} = -\tilde{\psi}_{j,j} \quad (j = 1, 2),$$
 (2.18)

and

$$\tilde{\phi}_{2,t} - \frac{1}{J_2} (\tilde{x}_{2,2} \tilde{x}_{2,t} + \tilde{y}_{2,2} \tilde{y}_{2,t}) \tilde{\phi}_{2,2} + \frac{1}{2} \frac{1}{J_2} (\tilde{\phi}_{2,2}^2 - \tilde{\psi}_{2,2}^2) + \frac{1}{c^2} \tilde{y}_2 - B(t)
= \frac{\rho_1}{\rho_2} \left\{ \tilde{\phi}_{1,t} - \frac{1}{J_1} (\tilde{x}_{1,1} \tilde{x}_{1,t} + \tilde{y}_{1,1} \tilde{y}_{1,t}) \tilde{\phi}_{1,1} + \frac{1}{2} \frac{1}{J_1} (\tilde{\phi}_{1,1}^2 - \tilde{\psi}_{1,1}^2) + \frac{1}{c^2} \tilde{y}_1 \right\}, \quad (2.19)$$

where the notation for the derivatives in (2.10) has been used. Here, note that $\xi_j = \xi_j(\hat{\xi}, t)$ at the interface $\eta_j = 0$ (j = 1, 2) are given by (2.14). The conditions at infinities (2.8) are

satisfied with

$$z_1 \to \zeta_1 \quad \text{and} \quad f_1 \to \zeta_1 \quad \text{as } \eta_1 \to \infty z_2 \to \zeta_2 \quad \text{and} \quad f_2 \to \zeta_2 \quad \text{as } \eta_2 \to -\infty$$
 (2.20)

The analyticity of $z_j = x_j + iy_j$ and $f_j = \phi_j + i\psi_j$ (j = 1, 2) with (2.20) yields the relations between the real and imaginary parts at the interface as

$$\tilde{x}_1 - \xi_1 = \mathcal{H}_1[\tilde{y}_1], \quad \tilde{\psi}_1 = -\mathcal{H}_1[\tilde{\phi}_1 - \xi_1], \quad \tilde{x}_2 - \xi_2 = -\mathcal{H}_2[\tilde{y}_2], \quad \tilde{\psi}_2 = \mathcal{H}_2[\tilde{\phi}_2 - \xi_2],$$
(2.21*a-d*)

where $\mathcal{H}_j[F]$ is the Hilbert transform for a real-valued function $F = F(\xi_j)$ in the ζ_j -plane (j = 1, 2) defined by

$$\mathcal{H}_{j}[F](\xi_{j}) := \frac{1}{\pi} \text{P.V.} \int_{-\infty}^{\infty} \frac{F(\xi_{j}')}{\xi_{j}' - \xi_{j}} \, \mathrm{d}\xi_{j}' \quad (j = 1, 2), \tag{2.22}$$

with P.V. denoting Cauchy's principal value. Thus the governing equations (2.16), (2.17), (2.18) (j = 1 or 2) and (2.19) determine the five unknown variables \tilde{y}_i , $\tilde{\phi}_i$ (j = 1, 2) and γ .

3. Steady interfacial waves of symmetric profile

We write steady solutions for 2π -periodic interfacial waves as

$$z_{j} = z_{j}^{(0)}(\zeta_{j}) = x_{j}^{(0)}(\xi_{j}, \eta_{j}) + iy_{j}^{(0)}(\xi_{j}, \eta_{j})$$

$$f_{j} = f_{j}^{(0)}(\zeta_{j}) = \phi_{j}^{(0)}(\xi_{j}, \eta_{j}) + i\psi_{j}^{(0)}(\xi_{j}, \eta_{j})$$

$$(j = 1, 2),$$

$$(3.1)$$

and ξ_1 and ξ_2 at the interface as

$$\xi_1 = \xi_1^{(0)}(\hat{\xi}) = \hat{\xi} + \gamma^{(0)}(\hat{\xi}) \quad \text{and} \quad \xi_2 = \xi_2^{(0)}(\hat{\xi}) = \hat{\xi} - \gamma^{(0)}(\hat{\xi}) \quad \text{for } -\pi \leqslant \hat{\xi} \leqslant \pi,$$
(3.2)

with
$$\xi_j^{(0)}(\hat{\xi} = \pm \pi) = \pm \pi \ (j = 1, 2) \text{ and } \gamma^{(0)}(\hat{\xi} = \pm \pi) = 0.$$

We assume that the steady wave profile is symmetric with respect to the vertical line passing through the wave crest. Then, we numerically obtain the steady wave solutions using the method of computation summarized in Appendix A. As the steady limit of our unsteady formulation can be reduced to the steady formulation of Saffman & Yuen (1982), the numerical method for steady solutions is similar to theirs. In this method, the steady wave solutions are approximated by truncated Fourier series with N terms, as shown in (A4) with (A5). We found that this method of computation with N = 128 produces reliable steady solutions for the ranges of the density ratio ρ_1/ρ_2 and the wave steepness h that we choose in this work, as discussed in Appendix A.

Figure 2(a) exhibits computed steady wave profiles with N=128 for the density ratios $\rho_1/\rho_2=0.1$ and 0.9 with varying wave steepness h. The corresponding fifth-order approximate solutions of Tsuji & Nagata (1973) are shown in figure 2(b). From these, we can see that the computed wave profile near the crest of large-amplitude interfacial waves becomes rounded as ρ_1/ρ_2 increases, and that the accuracy of the approximate fifth-order solutions in figure 2(b) deteriorates as h increases.

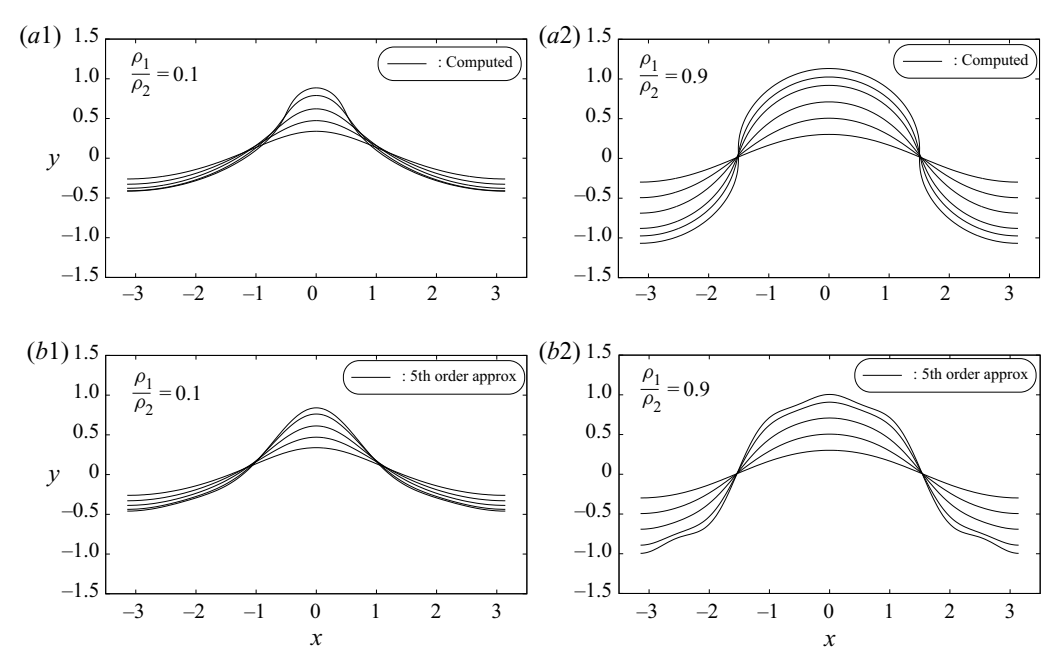


Figure 2. Wave profiles of steady interfacial waves of symmetric profile for different values of the wave steepness h. The density ratios used for the left and right panels are $\rho_1/\rho_2 = 0.1$ and 0.9, respectively. (a) Fully nonlinear solutions computed using the present method with N = 128: (a1) h = 0.6, 0.8, 1.0, 1.2, 1.3; (a2) h = 0.6, 1.0, 1.4, 1.8, 2.0, 2.2. (b) Fifth-order approximate solutions (Tsuji & Nagata 1973): (b1) h = 0.6, 0.8, 1.0, 1.2, 1.3; (b2) h = 0.6, 1.0, 1.4, 1.8, 2.0.

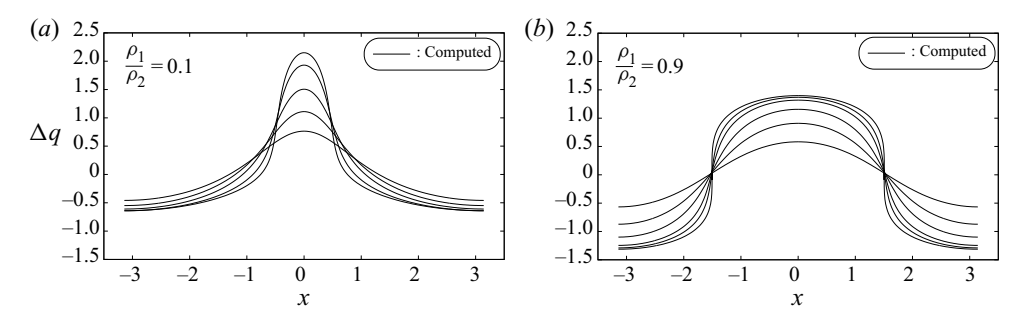


Figure 3. The tangential velocity jump Δq at the interface defined by (3.3) for different values of the density ratio ρ_1/ρ_2 and the wave steepness h: (a) $\rho_1/\rho_2 = 0.1$, h = 0.6, 0.8, 1.0, 1.2, 1.3; (b) $\rho_1/\rho_2 = 0.9$, h = 0.6, 1.0, 1.4, 1.8, 2.0, 2.2. Each solution is computed using the present method with N = 128.

Figure 3 shows the tangential velocity jump Δq across the interface of steady interfacial waves, which is defined as

$$\Delta q = \operatorname{sgn}(\Delta u) \sqrt{\Delta u^2 + \Delta v^2},\tag{3.3}$$

where $\Delta u = u_1^{(0)} - u_2^{(0)}$, $\Delta v = v_1^{(0)} - v_2^{(0)}$ and $\operatorname{sgn}(\Delta u)$ denotes the sign of Δu . Here, $u_j^{(0)} = \phi_{j,x}^{(0)} = \tilde{x}_{j,j}^{(0)}/J_j^{(0)}$ and $v_j^{(0)} = \phi_{j,y}^{(0)} = \tilde{y}_{j,j}^{(0)}/J_j^{(0)}$ are the horizontal and vertical velocities at the interface in the ζ_j -plane (j=1,2), respectively. The resulting discontinuity of the tangential velocity causes the wave-induced KH instability.

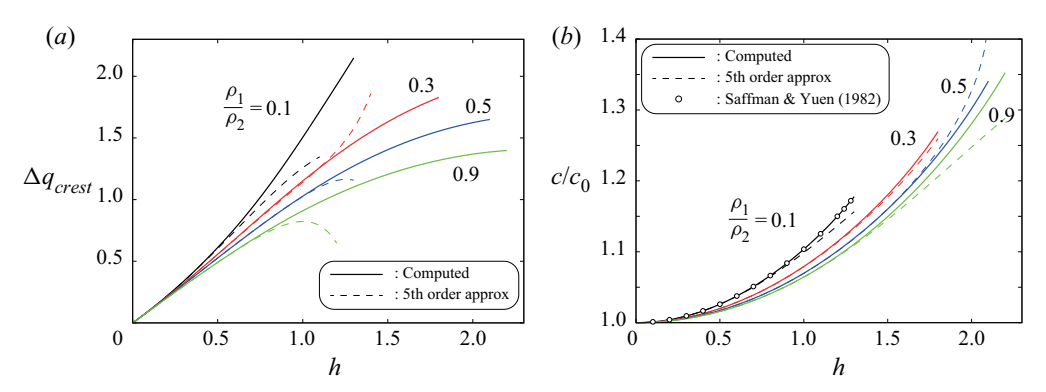


Figure 4. Variation with wave steepness h of the tangential velocity jump Δq_{crest} at the wave crest and the wave speed c of steady interfacial waves normalized by the linear wave speed c_0 given by (3.4). The computed results using the present method with N=128 (solid lines) are compared with the fifth-order approximate solutions (Tsuji & Nagata 1973) (dashed lines) and the computed results of Saffman & Yuen (1982) for $\rho_1/\rho_2=0.1$ (circles). The density ratios used for computations are $\rho_1/\rho_2=0.1$ (black), 0.3 (red), 0.5 (blue) and 0.9 (green).

Figures 4(a) and 4(b) show the variation of the tangential velocity jump Δq_{crest} at the wave crest and the wave speed c of the steady waves with the wave steepness h, respectively, for the density ratios $\rho_1/\rho_2 = 0.1$, 0.3, 0.5 and 0.9. In figure 4(b), c is normalized by the (dimensionless) linear wave speed c_0 given by

$$c_0 = \sqrt{\frac{\rho_2 - \rho_1}{\rho_2 + \rho_1}} = \sqrt{\frac{1 - \rho_1/\rho_2}{1 + \rho_1/\rho_2}}.$$
 (3.4)

It is shown that the computed result of c/c_0 for $\rho_1/\rho_2=0.1$ agrees well with that of Saffman & Yuen (1982). To compute the results (solid lines), we choose N=128 and increase h until the error tolerance (A8) is no longer satisfied, or the convergence of each Fourier coefficient in (A4) is too slow. Thus the right end of each solid line does not represent the limiting wave, but we focus on the range of $h \le 1$ in this work. In addition, these figures show that the fifth-order approximate solutions (dashed lines) of Tsuji & Nagata (1973) agree with our computed results only for small values of h. The results for Δq_{crest} and c/c_0 will be used in §§ 5 and 6 to estimate the critical condition for instability and the growth rates.

4. Linear stability analysis

4.1. Linearization around steady wave solutions in the ζ_1 - and ζ_2 -planes

For linear stability analysis, we superimpose time-dependent small-amplitude disturbances $z_j^{(1)}(\zeta_j,t), f_j^{(1)}(\zeta_j,t)$ and $\gamma^{(1)}(\hat{\xi},t)$ on the steady wave solutions $z_j^{(0)}(\zeta_j), f_j^{(0)}(\zeta_j)$ and $\gamma^{(0)}(\hat{\xi})$, respectively, as

$$z_{j}(\zeta_{j}, t) = z_{j}^{(0)}(\zeta_{j}) + z_{j}^{(1)}(\zeta_{j}, t)$$

$$f_{j}(\zeta_{j}, t) = f_{j}^{(0)}(\zeta_{j}) + f_{j}^{(1)}(\zeta_{j}, t)$$

$$(j = 1, 2) \text{ and } \gamma(\hat{\xi}, t) = \gamma^{(0)}(\hat{\xi}) + \gamma^{(1)}(\hat{\xi}, t),$$

$$(4.1)$$

and linearize the governing equations around the steady wave solutions. Note that $z_j^{(1)}(\zeta_j, t)$ and $f_j^{(1)}(\zeta_j, t)$ are both analytic in the ζ_j -plane (j = 1, 2). Similarly to (2.9), we write the

disturbances at the interface as

$$\tilde{x}_{j}^{(1)}(\xi_{j},t) = x_{j}^{(1)}(\xi_{j},\eta_{j}=0,t), \quad \tilde{y}_{j}^{(1)}(\xi_{j},t) = y_{j}^{(1)}(\xi_{j},\eta_{j}=0,t)
\tilde{\phi}_{j}^{(1)}(\xi_{j},t) = \phi_{j}^{(1)}(\xi_{j},\eta_{j}=0,t), \quad \tilde{\psi}_{j}^{(1)}(\xi_{j},t) = \psi_{j}^{(1)}(\xi_{j},\eta_{j}=0,t)$$
(4.2)

We look for solutions of the linearized equations in the form of

$$\tilde{x}_{j}^{(1)}(\xi_{j},t) = e^{\sigma t} \check{x}_{j}^{(1)}(\xi_{j}), \quad \tilde{y}_{j}^{(1)}(\xi_{j},t) = e^{\sigma t} \check{y}_{j}^{(1)}(\xi_{j})
\tilde{\phi}_{j}^{(1)}(\xi_{j},t) = e^{\sigma t} \check{\phi}_{j}^{(1)}(\xi_{j}), \quad \tilde{\psi}_{j}^{(1)}(\xi_{j},t) = e^{\sigma t} \check{\psi}_{j}^{(1)}(\xi_{j})$$

$$(j = 1, 2), \qquad (4.3)$$

and

$$\gamma^{(1)}(\hat{\xi}, t) = e^{\sigma t} \dot{\gamma}^{(1)}(\hat{\xi}), \tag{4.4}$$

where $\sigma = \sigma_r + i\sigma_i \in \mathbb{C}$. The steady interfacial waves are linearly unstable if and only if there exists a positive real part $\sigma_r > 0$. Notice that this condition is equivalent to the existence of any real part as both σ and $-\bar{\sigma}$ are eigenvalues to be discussed later, where $\bar{\sigma}$ denotes the complex conjugate of σ .

Substituting these into the governing equations (2.18) for j = 1, (2.19), (2.16) and (2.17), and expanding them around the steady wave solutions and $\xi_j = \xi_j^{(0)}(\hat{\xi})$ (j = 1, 2), we can obtain the linearized equations for $\check{x}_i^{(1)}$, $\check{y}_i^{(1)}$, $\check{\phi}_j^{(1)}$, $\check{\psi}_j^{(1)}$ (j = 1, 2) and $\check{\gamma}^{(1)}$ as follows:

$$\sigma(\tilde{\mathbf{x}}_{1.1}^{(0)}\dot{\mathbf{y}}_{1}^{(1)} - \tilde{\mathbf{y}}_{1.1}^{(0)}\dot{\mathbf{x}}_{1}^{(1)}) = -\dot{\boldsymbol{\psi}}_{1.1}^{(1)},\tag{4.5}$$

$$\begin{split} \sigma \left\{ \check{\phi}_{2}^{(1)} - \frac{1}{J_{2}^{(0)}} (\tilde{x}_{2,2}^{(0)} \check{x}_{2}^{(1)} + \tilde{y}_{2,2}^{(0)} \check{y}_{2}^{(1)}) \right\} + \frac{1}{J_{2}^{(0)}} \check{\phi}_{2,2}^{(1)} - \frac{1}{(J_{2}^{(0)})^{2}} (\tilde{x}_{2,2}^{(0)} \check{x}_{2,2}^{(1)} + \tilde{y}_{2,2}^{(0)} \check{y}_{2,2}^{(1)}) \\ + \frac{1}{c^{2}} \check{y}_{2}^{(1)} + \left\{ \frac{\frac{1}{2} J_{2,2}^{(0)}}{(J_{2}^{(0)})^{2}} - \frac{1}{c^{2}} \tilde{y}_{2,2}^{(0)} \right\} \check{\gamma}^{(1)} \\ = \frac{\rho_{1}}{\rho_{2}} \left[\sigma \left\{ \check{\phi}_{1}^{(1)} - \frac{1}{J_{1}^{(0)}} (\tilde{x}_{1,1}^{(0)} \check{x}_{1}^{(1)} + \tilde{y}_{1,1}^{(0)} \check{y}_{1}^{(1)}) \right\} + \frac{1}{J_{1}^{(0)}} \check{\phi}_{1,1}^{(1)} - \frac{1}{(J_{1}^{(0)})^{2}} (\tilde{x}_{1,1}^{(0)} \check{x}_{1,1}^{(1)} + \tilde{y}_{1,1}^{(0)} \check{y}_{1,1}^{(1)}) \\ + \frac{1}{c^{2}} \check{y}_{1}^{(1)} - \left\{ \frac{\frac{1}{2} J_{1,1}^{(0)}}{(J_{1}^{(0)})^{2}} - \frac{1}{c^{2}} \tilde{y}_{1,1}^{(0)} \right\} \check{\gamma}^{(1)} \right\}, \end{split}$$
(4.6)

$$\check{x}_{1}^{(1)} - \check{x}_{2}^{(1)} = -(\tilde{x}_{1,1}^{(0)} + \tilde{x}_{2,2}^{(0)})\check{\gamma}^{(1)},$$
(4.7)

$$\check{y}_{1}^{(1)} - \check{y}_{2}^{(1)} = -(\tilde{y}_{1.1}^{(0)} + \tilde{y}_{2.2}^{(0)})\check{\gamma}^{(1)}, \tag{4.8}$$

$$\check{\psi}_1^{(1)}(\xi_1 = \xi_1^{(0)}(\hat{\xi})) = \check{\psi}_2^{(1)}(\xi_2 = \xi_2^{(0)}(\hat{\xi})),\tag{4.9}$$

where $\xi_j = \xi_j^{(0)}(\hat{\xi})$ (j = 1, 2) at the interface are given by (3.2). In addition, eliminating $\gamma^{(1)}$ from the contact conditions (4.7) and (4.8), we obtain

$$(\tilde{y}_{1,1}^{(0)} + \tilde{y}_{2,2}^{(0)})\tilde{x}_{1}^{(1)} - (\tilde{x}_{1,1}^{(0)} + \tilde{x}_{2,2}^{(0)})\tilde{y}_{1}^{(1)} = (\tilde{y}_{1,1}^{(0)} + \tilde{y}_{2,2}^{(0)})\tilde{x}_{2}^{(1)} - (\tilde{x}_{1,1}^{(0)} + \tilde{x}_{2,2}^{(0)})\tilde{y}_{2}^{(1)}. \tag{4.10}$$

For later convenience, we use (4.10) instead of (4.8). Five equations (4.5), (4.6), (4.7), (4.9) and (4.10) determine the linear stability of steady interfacial waves.

Following Floquet theory, we can write the general solutions of (4.5), (4.6), (4.7), (4.9) and (4.10) in the form of

$$\tilde{x}_{j}^{(1)}(\xi_{j}) = e^{ip\xi_{j}} \sum_{m=-\infty}^{\infty} \alpha_{jm}^{(1)} e^{im\xi_{j}}, \quad \tilde{y}_{j}^{(1)}(\xi_{j}) = e^{ip\xi_{j}} \sum_{m=-\infty}^{\infty} a_{jm}^{(1)} e^{im\xi_{j}}
\tilde{\phi}_{j}^{(1)}(\xi_{j}) = e^{ip\xi_{j}} \sum_{m=-\infty}^{\infty} b_{jm}^{(1)} e^{im\xi_{j}}, \quad \tilde{\psi}_{j}^{(1)}(\xi_{j}) = e^{ip\xi_{j}} \sum_{m=-\infty}^{\infty} \beta_{jm}^{(1)} e^{im\xi_{j}}
(4.11)$$

and

$$\check{\gamma}^{(1)}(\hat{\xi}) = e^{ip\hat{\xi}} \sum_{m=-\infty}^{\infty} c_m^{(1)} e^{im\hat{\xi}}, \tag{4.12}$$

where the exponent p is assumed to be real so that the solutions are bounded for $-\infty < \xi_j < \infty$ (j=1,2). Since the linearized equations (4.5), (4.6), (4.7), (4.9) and (4.10) are invariant under the transformation $\xi_j \to -\xi_j$, $\check{\phi}_j^{(1)} \to -\check{\phi}_j^{(1)}$, $\check{\psi}_j^{(1)} \to -\check{\psi}_j^{(1)}$ (j=1,2), $\hat{\xi} \to -\hat{\xi}, t \to -t$ and $\gamma^{(1)} \to -\gamma^{(1)}$, there is a degeneracy in the choice of p, similarly to the case of surface waves (for e.g. see Tiron & Choi (2012, § 2.4) and Murashige & Choi (2020, § 4.3)). In particular, if σ is an eigenvalue for p, then $-\bar{\sigma}$ is another eigenvalue for the same value of p, and $\bar{\sigma}$ and $-\sigma$ are the eigenvalues for 1-p. Thus the range of p can be restricted to $0 \le p \le 1/2$. In addition, from the analyticity given by (2.21a-d) and the following relations for the Hilbert transform

$$\mathcal{H}_{j}[e^{i\nu\xi_{j}}] = i\operatorname{sgn}(\nu) e^{i\nu\xi_{j}} \quad (j = 1, 2) \text{ with } \operatorname{sgn}(\nu) = \begin{cases} +1 & (\nu > 0) \\ 0 & (\nu = 0) \\ -1 & (\nu < 0) \end{cases}$$
(4.13)

the coefficients $\alpha_{jm}^{(1)}$ and $\beta_{jm}^{(1)}$ (j=1,2) in (4.11) can be related to $a_{jm}^{(1)}$ and $b_{jm}^{(1)}$, respectively, by

$$\alpha_{1m}^{(1)} = i \operatorname{sgn}(p+m) \, a_{1m}^{(1)}, \qquad \beta_{1m}^{(1)} = -i \operatorname{sgn}(p+m) \, b_{1m}^{(1)}$$

$$\alpha_{2m}^{(1)} = -i \operatorname{sgn}(p+m) \, a_{2m}^{(1)}, \qquad \beta_{2m}^{(1)} = i \operatorname{sgn}(p+m) \, b_{2m}^{(1)}$$

$$(4.14)$$

Substituting these into the linearized equations (4.5), (4.6), (4.7), (4.9) and (4.10), we obtain

$$\sigma \sum_{m=-\infty}^{\infty} A_{11,m}(\hat{\xi}) a_{1m}^{(1)} = \sum_{m=-\infty}^{\infty} B_{11,m}(\hat{\xi}) b_{1m}^{(1)}, \tag{4.15}$$

$$\sigma \sum_{m=-\infty}^{\infty} \{A_{21,m}(\hat{\xi})a_{1m}^{(1)} + A_{22,m}(\hat{\xi})a_{2m}^{(1)} + B_{21,m}(\hat{\xi})b_{1m}^{(1)} + B_{22,m}(\hat{\xi})b_{2m}^{(1)}\}$$

$$= \sum_{m=-\infty}^{\infty} \{A_{31,m}(\hat{\xi})a_{1m}^{(1)} + A_{32,m}(\hat{\xi})a_{2m}^{(1)} + B_{31,m}(\hat{\xi})b_{1m}^{(1)} + B_{32,m}(\hat{\xi})b_{2m}^{(1)} + C_{3,m}(\hat{\xi})c_{m}^{(1)}\},$$
(4.16)

$$\sum_{m=-\infty}^{\infty} A_{41,m}(\hat{\xi}) a_{1m}^{(1)} + \sum_{m=-\infty}^{\infty} A_{42,m}(\hat{\xi}) a_{2m}^{(1)} = \sum_{m=-\infty}^{\infty} C_{4,m}(\hat{\xi}) c_m^{(1)}, \tag{4.17}$$

$$\sum_{m=-\infty}^{\infty} A_{51,m}(\hat{\xi}) a_{1m}^{(1)} = \sum_{m=-\infty}^{\infty} A_{52,m}(\hat{\xi}) a_{2m}^{(1)} \quad \text{and} \quad \sum_{m=-\infty}^{\infty} B_{51,m}(\hat{\xi}) b_{1m}^{(1)} = \sum_{m=-\infty}^{\infty} B_{52,m}(\hat{\xi}) b_{2m}^{(1)},$$
(4.18*a,b*)

where $A_{*,m}(\hat{\xi})$, $B_{*,m}(\hat{\xi})$ and $C_{*,m}(\hat{\xi})$ are 2π -periodic functions determined by the steady wave solutions and summarized in Appendix B. Furthermore, from periodicity, the coefficient functions $A_{*,m}(\hat{\xi})$, $B_{*,m}(\hat{\xi})$ and $C_{*,m}(\hat{\xi})$ can be expanded in the form of Fourier series as

$$A_{*,m}(\hat{\xi}) = \sum_{k=-\infty}^{\infty} A_{*,km} e^{ik\hat{\xi}}, \quad B_{*,m}(\hat{\xi}) = \sum_{k=-\infty}^{\infty} B_{*,km} e^{ik\hat{\xi}}, \quad C_{*,m}(\hat{\xi}) = \sum_{k=-\infty}^{\infty} C_{*,km} e^{ik\hat{\xi}}.$$

$$(4.19a-c)$$

Then, we can transform (4.15), (4.16), (4.17) and (4.18a,b) into

$$\sigma \sum_{m=-\infty}^{\infty} A_{11,km} a_{1m}^{(1)} = \sum_{m=-\infty}^{\infty} B_{11,km} b_{1m}^{(1)}, \tag{4.20}$$

$$\sigma \sum_{m=-\infty}^{\infty} \{A_{21,km} a_{1m}^{(1)} + A_{22,km} a_{2m}^{(1)} + B_{21,km} b_{1m}^{(1)} + B_{22,km} b_{2m}^{(1)}\}$$

$$= \sum_{m=-\infty}^{\infty} \{A_{31,km}a_{1m}^{(1)} + A_{32,km}a_{2m}^{(1)} + B_{31,km}b_{1m}^{(1)} + B_{32,km}b_{2m}^{(1)} + C_{3,km}c_m^{(1)}\}, \quad (4.21)$$

$$\sum_{m=-\infty}^{\infty} A_{41,km} a_{1m}^{(1)} + \sum_{m=-\infty}^{\infty} A_{42,km} a_{2m}^{(1)} = \sum_{m=-\infty}^{\infty} C_{4,km} c_m^{(1)}, \tag{4.22}$$

$$\sum_{m=-\infty}^{\infty} A_{51,km} a_{1m}^{(1)} = \sum_{m=-\infty}^{\infty} A_{52,km} a_{2m}^{(1)} \quad \text{and} \quad \sum_{m=-\infty}^{\infty} B_{51,km} b_{1m}^{(1)} = \sum_{m=-\infty}^{\infty} B_{52,km} b_{2m}^{(1)},$$
(4.23*a,b*)

for all $k \in \mathbb{Z}$. These equations (4.20), (4.21), (4.22) and (4.23a,b) determine σ , $a_{jm}^{(1)}$ and $b_{jm}^{(1)}$ (j = 1, 2). In particular, in the limit of wave steepness $h \to 0$, we can analytically obtain the expression of σ , in terms of the exponent p and the mode number m, as

$$\sigma \to \sigma_{p,m}^{\pm} := i\{-(p+m) \pm \sqrt{|p+m|}\} \text{ as } h \to 0.$$
 (4.24)

Here, note that this limit $\sigma_{p,m}^{\pm}$ is independent of the density ratio ρ_1/ρ_2 .

4.2. The method of computation

First, we can numerically determine the Fourier coefficients $A_{*,km}$, $B_{*,km}$ and $C_{*,km}$ (k, m = -N, ..., N-1) in (4.19a-c) using the steady wave solutions at $\hat{\xi} = \hat{\xi}_{\ell} = \ell \pi/N$ $(\ell = -N, ..., N)$ obtained in § 3 and the fast Fourier transform. Here, N is the total

number of terms of the truncated Fourier series (A5) for the steady wave solutions. Next, we substitute these Fourier coefficients into (4.19a-c), (4.20), (4.21), (4.22) and (4.23a,b), and truncate the resulting infinite series as

$$\sum_{k=-\infty}^{\infty} \sim \sum_{k=-M}^{M} \quad \text{and} \quad \sum_{m=-\infty}^{\infty} \sim \sum_{m=-M}^{M} \quad \text{with } M < N.$$
 (4.25)

To reduce numerical errors, large-wavenumber components are filtered out by setting M < N. Then (4.20), (4.21), (4.22) and (4.23a,b) can be rewritten, respectively, as

$$\sigma \mathbf{A}_{11} a_1^{(1)} = \mathbf{B}_{11} b_1^{(1)}, \tag{4.26}$$

$$\sigma(\mathbf{A}_{21}\mathbf{a}_1^{(1)} + \mathbf{A}_{22}\mathbf{a}_2^{(1)} + \mathbf{B}_{21}\mathbf{b}_1^{(1)} + \mathbf{B}_{22}\mathbf{b}_2^{(1)})$$

$$= \mathbf{A}_{31}\mathbf{a}_{1}^{(1)} + \mathbf{A}_{32}\mathbf{a}_{2}^{(1)} + \mathbf{B}_{31}\mathbf{b}_{1}^{(1)} + \mathbf{B}_{32}\mathbf{b}_{2}^{(1)} + \mathbf{C}_{3}\mathbf{c}^{(1)}, \tag{4.27}$$

$$\mathbf{A}_{41}a_1^{(1)} + \mathbf{A}_{42}a_2^{(1)} = \mathbf{C}_4c^{(1)}, \tag{4.28}$$

$$\mathbf{A}_{51}\mathbf{a}_{1}^{(1)} = \mathbf{A}_{52}\mathbf{a}_{2}^{(1)}$$
 and $\mathbf{B}_{51}\mathbf{b}_{1}^{(1)} = \mathbf{B}_{52}\mathbf{b}_{2}^{(1)}$, (4.29*a*,*b*)

where $\mathbf{A}_* = (A_{*,km})_{k,m=-M}^M$, $\mathbf{B}_* = (B_{*,km})_{k,m=-M}^M$ and $\mathbf{C}_* = (C_{*,km})_{k,m=-M}^M$ are $(2M+1) \times (2M+1)$ matrices, and $\mathbf{a}_j^{(1)} = (a_{jm}^{(1)})_{m=-M}^M$, $\mathbf{b}_j^{(1)} = (b_{jm}^{(1)})_{m=-M}^M$ and $\mathbf{c}^{(1)} = (c_m^{(1)})_{m=-M}^M$ (j=1,2) are vectors with 2M+1 components. Furthermore, from (4.28) and (4.29a,b), we can represent $\mathbf{a}_2^{(1)}$, $\mathbf{b}_2^{(1)}$ and $\mathbf{c}_3^{(1)}$ by $\mathbf{a}_3^{(1)}$ and $\mathbf{b}_3^{(1)}$ as

$$a_2^{(1)} = \mathbf{A}_{53} a_1^{(1)}, \quad b_2^{(1)} = \mathbf{B}_{53} b_1^{(1)}, \quad c^{(1)} = \mathbf{C}_5 a_1^{(1)},$$
 (4.30*a*-*c*)

where

$$\mathbf{A}_{53} = \mathbf{A}_{52}^{-1} \mathbf{A}_{51}, \quad \mathbf{B}_{53} = \mathbf{B}_{52}^{-1} \mathbf{B}_{51}, \quad \mathbf{C}_5 = \mathbf{C}_4^{-1} (\mathbf{A}_{41} + \mathbf{A}_{42} \mathbf{A}_{53}).$$
 (4.31*a-c*)

Substituting these into (4.26) and (4.27), we obtain

$$\sigma \begin{pmatrix} \mathbf{A}_{11} & \mathbf{0} \\ \mathbf{A}_{23} & \mathbf{B}_{23} \end{pmatrix} \begin{pmatrix} \mathbf{a}_{1}^{(1)} \\ \mathbf{b}_{1}^{(1)} \end{pmatrix} = \begin{pmatrix} \mathbf{0} & \mathbf{B}_{11} \\ \mathbf{A}_{33} & \mathbf{B}_{33} \end{pmatrix} \begin{pmatrix} \mathbf{a}_{1}^{(1)} \\ \mathbf{b}_{1}^{(1)} \end{pmatrix}, \tag{4.32}$$

where

$$\mathbf{A}_{23} = \mathbf{A}_{21} + \mathbf{A}_{22}\mathbf{A}_{53}, \quad \mathbf{A}_{33} = \mathbf{A}_{31} + \mathbf{A}_{32}\mathbf{A}_{53} + \mathbf{C}_{3}\mathbf{C}_{5}
\mathbf{B}_{23} = \mathbf{B}_{21} + \mathbf{B}_{22}\mathbf{B}_{53}, \quad \mathbf{B}_{33} = \mathbf{B}_{31} + \mathbf{B}_{32}\mathbf{B}_{53}$$
(4.33)

This is a generalized eigenvalue problem for the eigenvalue σ and the eigenvector $(a_1^{(1)}, b_1^{(1)})$. When the density ratio ρ_1/ρ_2 , the steady wave steepness h and the exponent p of disturbances are given, we can solve (4.32). In this work, we numerically solve (4.32) using computational routines for eigenvalue problems in LAPACK (http://www.netlib.org/lapack/).

4.3. The dominant wavenumber of disturbances and classification of eigenvalues The generalized eigenvalue problem (4.32) produces 4M + 2 sets of the eigenvalue σ and the corresponding eigenvector $(a_1^{(1)}, b_1^{(1)})$. Here, as shown in (4.11) and (4.25), $a_1^{(1)} = (a_{1m}^{(1)})_{m=-M}^M$ and $b_1^{(1)} = (b_{1m}^{(1)})_{m=-M}^M$ are the truncated Fourier coefficient vectors

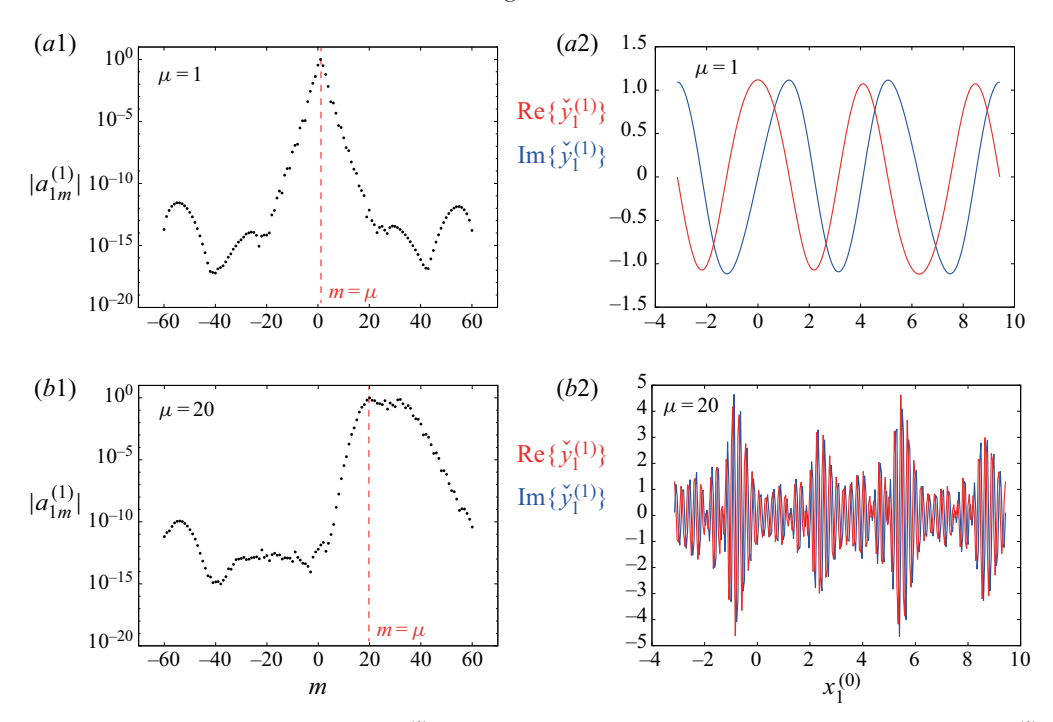


Figure 5. Examples of the variation of $|a_{1m}^{(1)}|$ with the mode number m and the corresponding disturbance $\check{y}_1^{(1)}$ for $\rho_1/\rho_2=0.9$, h=0.5 and p=1/2: (a) stable case ($\sigma_r\simeq 0.0$, $\sigma_i\simeq -0.257$) for which $\mu=1$; (b) unstable case ($\sigma_r\simeq 0.706$, $\sigma_i\simeq -24.7$) for which $\mu=20$. (a1) and (b1) show $|a_{1m}^{(1)}|$ for $\mu=1$ and 20, respectively. (a2) and (b2) show $\check{y}^{(1)}$ for $\mu=1$ and 20, respectively. The computed results are obtained using the present method with N=128 and M=60. The dominant mode number μ and the disturbance $\check{y}_1^{(1)}$ are defined by (4.34) and (4.11), respectively. The red and blue lines in (a2) and (b2) represent the real and imaginary parts of $\check{y}_1^{(1)}$, respectively.

for $\check{y}_1^{(1)}$ and $\check{\phi}_1^{(1)}$, respectively. For each eigenvalue σ , the disturbance has 2M+1 Fourier components, from which the dominant mode number μ is defined as the value of m at which the absolute value $|a_{1m}^{(1)}|$ is the maximum for $-M\leqslant m\leqslant M$, namely

$$\left| a_{1\mu}^{(1)} \right| = \max_{-M \leqslant m \leqslant M} \left| a_{1m}^{(1)} \right|. \tag{4.34}$$

An alternative is to use $|b_{1m}^{(1)}|$, but no difference is expected for the choice of μ . Note that μ is an integer and $-M \le \mu \le M$. Using this definition, 4M+2 eigenvalues are classified into the 2M+1 dominant mode groups. Then, as $\check{y}_1^{(1)}(\xi_1)$ can be expressed as

$$\check{\mathbf{y}}_{1}^{(1)}(\xi_{1}) = \sum_{m=-M}^{M} a_{1m}^{(1)} \exp(\mathrm{i}(m+p)\xi_{1}), \tag{4.35}$$

the dominant wavenumber of the disturbance $\check{y}_1^{(1)}$ is $\mu+p$ and, if $|a_{1\mu}^{(1)}|$ is much greater than $|a_{1m}^{(1)}|$ for all m $(m \neq \mu)$, we may approximate $\check{y}_1^{(1)}(\xi_1)$ as $\check{y}_1^{(1)}(\xi_1) \sim a_{1\mu}^{(1)} \exp(\mathrm{i}(\mu+p)\xi_1)$.

Figure 5 shows the variation of $|a_{1m}^{(1)}|$ with m and the corresponding disturbance $\check{y}_1^{(1)}$ for two eigenvalues. The physical and numerical parameters for these solutions are

 $\rho_1/\rho_2=0.9$, h=0.5, p=1/2, N=128 and M=60. One eigenvalue is for a stable mode ($\sigma_r\simeq 0.0$, $\sigma_i\simeq -0.257$) and the other is for an unstable mode ($\sigma_r\simeq 0.706$, $\sigma_i\simeq -24.7$). The results suggest that the dominant mode is well defined when its value is small, as shown in figure 5(a), but the bandwidth of $|a_{1m}^{(1)}|$ increases with $|\mu|$. For large $|\mu|$, there is some ambiguity in the definition of μ , as can be observed in figure 5(b). Furthermore, when $|\mu|$ is found large, the convergence of the Fourier series expansion for the corresponding disturbances in (4.11) and (4.12) becomes slow due to its truncation. Then M needs to be further increased, but, unfortunately, the computational cost increases with M. Therefore, for a fixed value of M, this causes a limitation of the classification of eigenvalues in terms of μ . Due to our limited computational resources, we choose N=128 and M=60, for which we focus on the modes of $|\mu|\leqslant 40$ for $h\leqslant 1$.

5. Approximations of the growth rate σ_r of the disturbances

We may analytically estimate the growth rate $\sigma_r = \text{Re}\{\sigma\}$ of the disturbances $z_j^{(1)}, f_j^{(1)}$ (j = 1, 2) and $\gamma^{(1)}$ to steady interfacial waves for two kinds of instability: (i) the wave-induced KH instability and (ii) the modulational instability.

5.1. Wave-induced KH instability

As described in § 1, after assuming that the velocity jump near the crest is locally constant, Pullin & Grimshaw (1985, (4.1) on p. 330) proposed the approximate growth rate of the wave-induced KH instability for interfacial waves using the well-known result of the KH instability for two horizontal uniform currents of different speed. Based on their approximation, the positive real part, or the growth rate $\sigma_r^{(KH)}$ of the wave-induced KH instability, can be written as

$$\sigma_r^{(\text{KH})} \sim \tilde{\sigma}_r^{(\text{KH})} = \text{Re}\left\{ \sqrt{(\mu + p)^2 \frac{\rho_1/\rho_2}{(1 + \rho_1/\rho_2)^2} (\Delta \tilde{q}_{crest})^2 - |\mu + p| \left(\frac{c_0}{\tilde{c}}\right)^2} \right\}, \quad (5.1)$$

where $\mu + p$ is the dominant wavenumber of disturbances defined by (4.34), $\Delta \tilde{q}_{crest}$ is the tangential velocity jump at the crest of the steady interfacial wave, \tilde{c} is the steady wave speed and c_0 is the linear wave speed given by (3.4). As $\Delta \tilde{q}_{crest}$ and \tilde{c} depend on the steady wave steepness h, the approximate growth rate $\tilde{\sigma}_r^{(KH)}$ changes with ρ_1/ρ_2 , h, μ and p.

In addition, (5.1) yields the critical mode number $\tilde{\mu}_c^{(KH)}$, at which the inside of the square root in (5.1) vanishes, as

$$\tilde{\mu}_c^{(KH)} := \frac{(1 + \rho_1/\rho_2)^2}{\rho_1/\rho_2} \frac{1}{(\Delta \tilde{q}_{crest})^2} \left(\frac{c_0}{\tilde{c}}\right)^2 - p. \tag{5.2}$$

For $\mu < \tilde{\mu}_c^{(\text{KH})}$ (> $\tilde{\mu}_c^{(\text{KH})}$), the steady interfacial wave is stable (unstable). Figure 6 shows the variation of $\tilde{\mu}_c^{(\text{KH})}$ with the steady wave steepness h for the exponent p = 1/2 and different values of the density ratio ρ_1/ρ_2 .

Note that $\sigma_r^{(\mathrm{KH})}$ and $\tilde{\mu}_c^{(\mathrm{KH})}$ can be estimated using either the fifth-order approximate solutions (Tsuji & Nagata 1973), or the fully nonlinear computed results for $\Delta \tilde{q}_{crest}$ and \tilde{c} . As can be seen in figure 6, the two results show little difference, except for $\rho_1/\rho_2=0.1$. Therefore, in § 6, the fifth-order approximate solutions are used for $\Delta \tilde{q}_{crest}$ and \tilde{c} as $\sigma_r^{(\mathrm{KH})}$ and $\tilde{\mu}_c^{(\mathrm{KH})}$ can be analytically estimated.

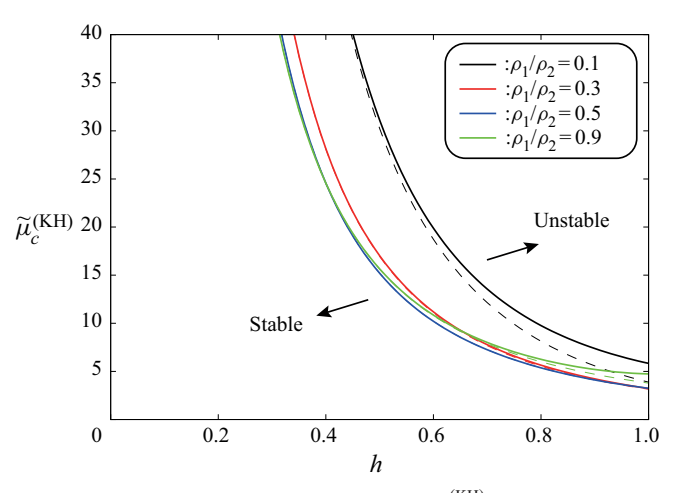


Figure 6. Variation of the approximate critical mode number $\tilde{\mu}_c^{(\text{KH})}$ given by (5.2) with the steady wave steepness h for p=1/2 and different values of the density ratio ρ_1/ρ_2 . In computing $\tilde{\mu}_c^{(\text{KH})}$, $\Delta \tilde{q}_{crest}$ and \tilde{c} in (5.2) are estimated using both the fifth-order approximate solutions of Tsuji & Nagata (1973) (solid) and the numerical solutions with N=128 (dashed).

5.2. Modulational instability

Introducing the slow space scale $X = \epsilon(x' + c_g t)$ and the slow time scale $\tau = \epsilon^2 t$ in the inertial frame (x', y', t) with x' = x - ct and y' = y, Grimshaw & Pullin (1985, (4.4), (4.8) and (4.9) on pp. 304–305) derived the nonlinear Schrödinger (NLS) equation for slowly modulated small-amplitude interfacial waves as

$$-iA_{\tau} + \alpha A_{XX} + \beta |A|^2 A = 0, \qquad (5.3)$$

with

$$c_g = \frac{1}{2}c_0, \quad \alpha = -\frac{1}{8}, \quad \beta = -\frac{1 + (\rho_1/\rho_2)^2}{2(1 + \rho_1/\rho_2)^2},$$
 (5.4)

where c_g denotes the group velocity, c_0 is given by (3.4) and $A = A(X, \tau)$ is the complex wave amplitude of the leading-order wave train. Following Mei, Stiassnie & Yue (2005, chap. 13), we can investigate the linear stability of the basic Stokes wave given by

$$A_0 = a_0 e^{-i\beta a_0^2 \tau} \quad (a_0 \in \mathbb{R}),$$
 (5.5)

which is the solution of $-iA_{0\tau} + \beta |A_0|^2 A_0 = 0$. In particular, the approximate growth rate $\tilde{\sigma}_r^{(NLS)}$ of disturbances for the modulational instability is given by

$$\tilde{\sigma}_r^{\text{(NLS)}} := \text{Re}\left\{ \frac{p}{8} \sqrt{2 \frac{1 + (\rho_1/\rho_2)^2}{(1 + \rho_1/\rho_2)^2} h^2 - p^2} \right\}.$$
 (5.6)

This is supposed to be valid for small values of h and p.

6. Numerical examples of linear stability analysis and discussion

This section summarizes the computed results for the eigenvalue $\sigma = \sigma_r + i\sigma_i$ of the generalized eigenvalue problem (4.32) using the present method described in §4.2,

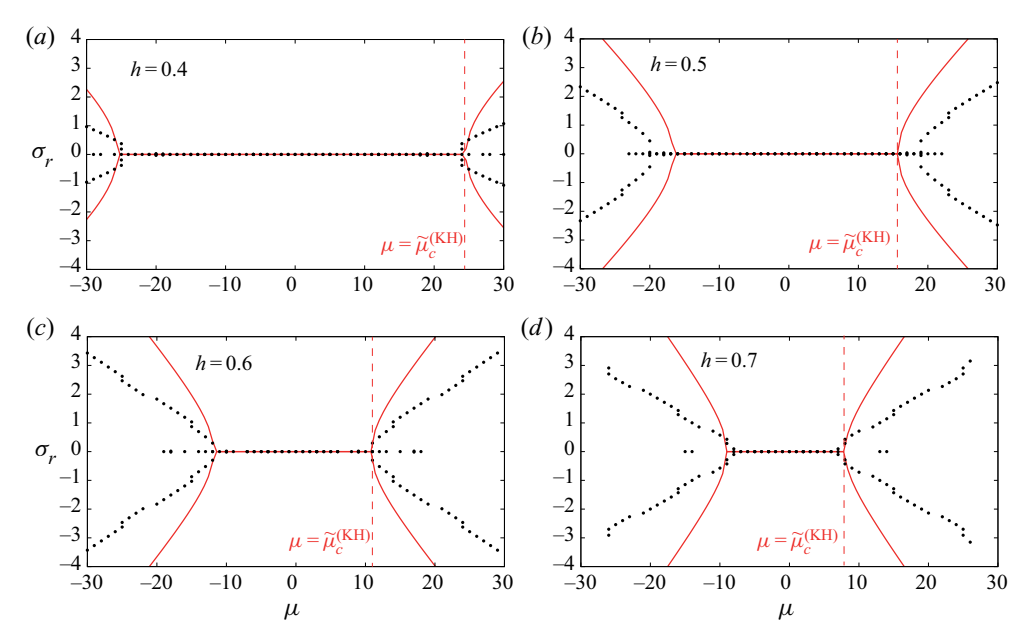


Figure 7. Variation of the growth rate σ_r with the dominant mode number μ of the corresponding disturbance for $\rho_1/\rho_2=0.9$, p=1/2 and different values of the wave steepness h. The computed results (dots) using the present method with N=128 and M=60 are compared with the approximate growth rate (red solid lines) $\tilde{\sigma}_r^{(\mathrm{KH})}$ given by (5.1). The red dashed line represents the approximate critical mode number $\tilde{\mu}_c^{(\mathrm{KH})}$ given by (5.2) for the wave-induced KH instability.

and discuss two kinds of instability: (i) the wave-induced KH instability and (ii) small-wavenumber instability including the modulational instability. The computed results in this section are obtained with N = 128 and M = 60, where N and M denote the total number of terms of the truncated Fourier series (A5) for steady wave solutions and (4.25) for disturbances, respectively.

6.1. Wave-induced KH instability

Figure 7 shows the variation of the growth rate σ_r with the dominant mode number μ for the density ratio $\rho_1/\rho_2=0.9$, the exponent p=1/2 and different values of the wave steepness: (a) h=0.4, (b) 0.5, (c) 0.6 and (d) 0.7. The computed results are compared with the approximate growth rate $\tilde{\sigma}_r^{(KH)}$ in (5.1) for the wave-induced KH instability. The computed results show that there exist unstable modes $(\sigma_r>0)$ for $|\mu|>\mu_c$, where μ_c is the critical mode number. This is analogous to the case of the well-known KH instability for two horizontal uniform currents of different speed. Since there are no background currents in this problem, the instability in figure 7 is the KH instability excited locally by the wave-induced tangential velocity jump. While its variation with μ is qualitatively similar to the computed results, the approximate growth rate $\tilde{\sigma}_r^{(KH)}$ in (5.1) is always overpredicted. Nevertheless, the critical mode number μ_c for the onset of the wave-induced KH instability is well approximated by $\tilde{\mu}_c^{(KH)}$ in (5.2). As the wave steepness increases, the critical mode number decreases, as can be seen in figure 7. For any wave steepness, as the growth rate increases with μ (> μ) and appears to be unbounded as $\mu \to \infty$, the inviscid initial value problem would be ill posed.

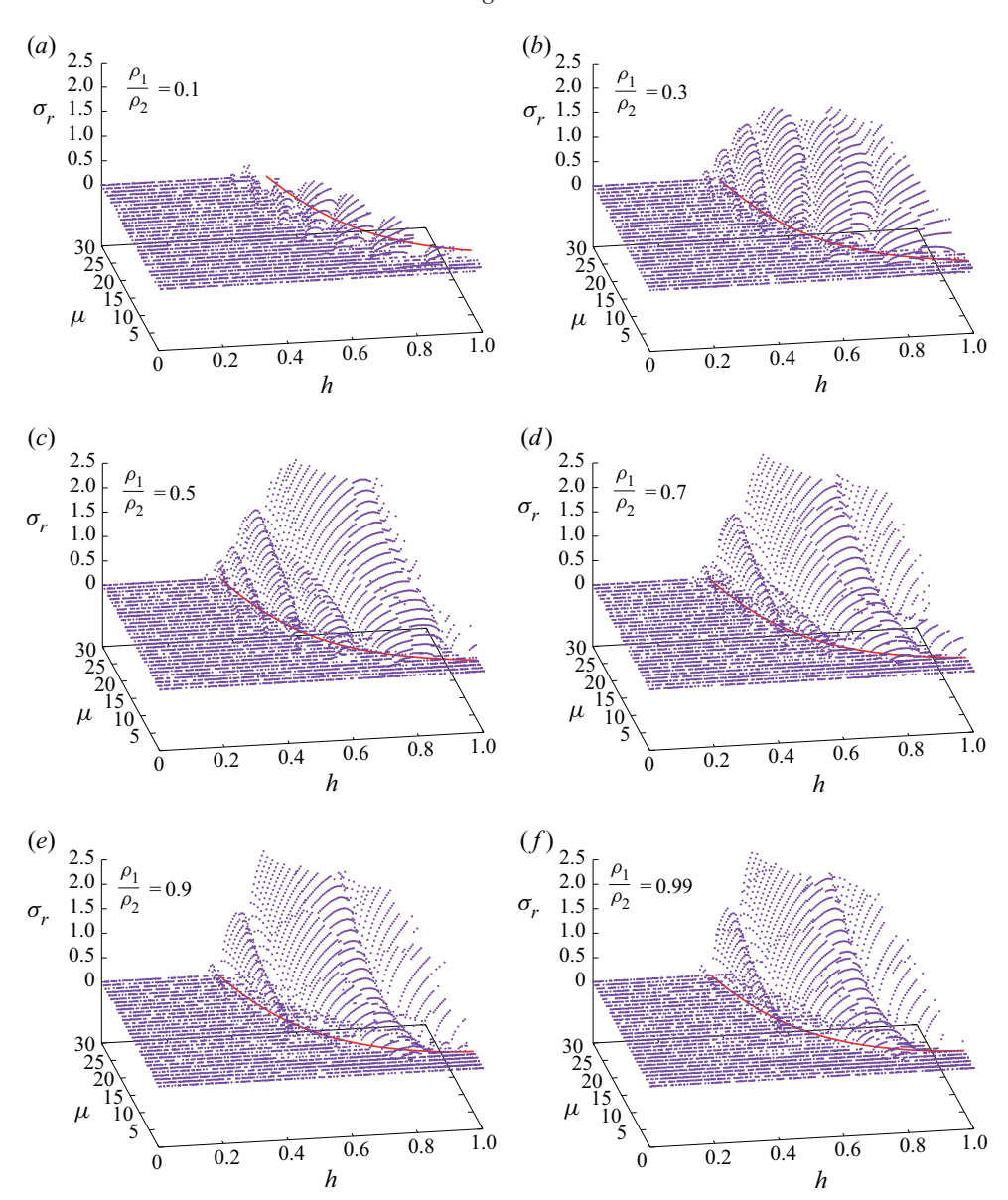


Figure 8. Variation of the growth rate σ_r with the steady wave steepness h and the dominant mode number μ of disturbances for different values of the density ratio ρ_1/ρ_2 (p=1/2). The computed results (blue dots) are obtained using the present method with N=128, M=60. The red solid line represents on the (μ , h)-plane the approximate critical mode number $\mu=\tilde{\mu}_c^{(KH)}(h)$ defined by (5.2).

Figure 8 shows the variation of the growth rate σ_r ($\geqslant 0$) with the wave steepness h and the dominant mode number μ for the exponent p=1/2 and different values of the density ratio: (a) $\rho_1/\rho_2=0.1$, (b) 0.3, (c) 0.5, (d) 0.7, (e) 0.9 and (f) 0.99. These three-dimensional plots allow us to observe the continuous change of σ_r with both h and μ simultaneously. The critical dominant wavenumber μ_c depends on the density ratio and the wave steepness, and the interfacial periodic steady waves are always unstable for $\mu > \mu_c$. We can observe that the value of the growth rate $\sigma_r > 0$ for the unstable range $\mu > \mu_c$ increases with the

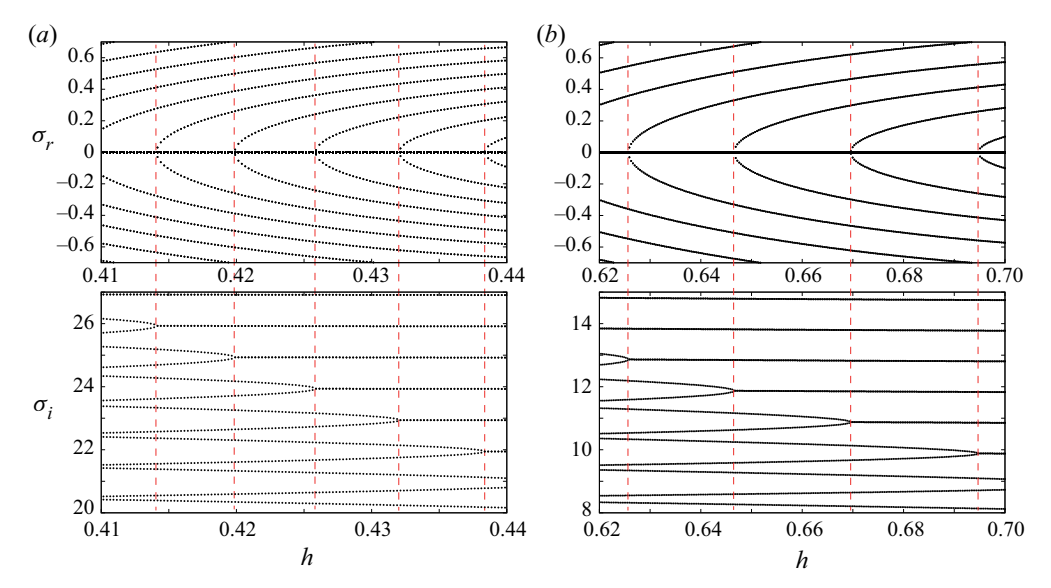


Figure 9. Variation of the real and imaginary parts of the eigenvalue $\sigma = \sigma_r + \mathrm{i}\sigma_i$ with the steady wave steepness h for $\rho_1/\rho_2 = 0.9$ and p = 1/2: (a) $0.41 \le h \le 0.44$; (b) $0.62 \le h \le 0.7$. The results (dots) are computed with N = 128 and M = 60. At the wave steepness h marked by the red dashed line, two eigenvalues collide and the growth rate σ_r changes from $\sigma_r = 0$ to $\sigma_r \ne 0$.

density ratio ρ_1/ρ_2 . However, the computed results vary little for $\rho_1/\rho_2 \geqslant 0.9$. It is found that the estimated critical curve $\mu = \tilde{\mu}_c^{(KH)}(h)$ approximately agrees with the computed results for $\rho_1/\rho_2 \geqslant 0.3$ but not for $\rho_1/\rho_2 = 0.1$. This disagreement for $\rho_1/\rho_2 = 0.1$ may be due to the fact that the tangential velocity jump near the crest for $\rho_1/\rho_2 = 0.1$ changes more rapidly than that for $\rho_1/\rho_2 \geqslant 0.3$, as shown in figure 3, and the tangential velocity jump cannot be assumed to be constant near the crest of the steady waves. Therefore, the approximate local analysis breaks down for small values of ρ_1/ρ_2 .

Figure 9 shows the variation of the real and imaginary parts of the eigenvalue $\sigma = \sigma_r + \mathrm{i}\sigma_i$ with the wave steepness h for the density ratio $\rho_1/\rho_2 = 0.9$, the exponent p = 1/2 and the dominant mode number $|\mu| \leq 40$. The computed results of the imaginary part σ_i demonstrate that some pairs of the eigenvalues collide successively at the wave steepness h shown by the red dashed lines. When two eigenvalues collide, the corresponding growth rate σ_r changes from $\sigma_r = 0$ to $\sigma_r \neq 0$, and the dominant mode number μ is equal to the critical mode number μ_c . These successive collisions of the eigenvalues result in the wave-induced KH instability found in figures 7 and 8. This observation is consistent with the previous theoretical results that the instability arises when two eigenvalues of opposite Krein signature or opposite energy sign collide, for example, in MacKay & Saffman (1986) for surface waves and Benjamin & Bridges (1997) for interfacial waves using Hamiltonian approaches.

In figures 7, 8 and 9, the value of the exponent p is fixed to p = 0.5. Figure 10 shows the variation of the growth rate σ_r with the wave steepness h and the dominant mode number μ for different values of the exponent p (the density ratio $\rho_1/\rho_2 = 0.9$). For relatively large values of $|\mu|$, the computed eigenvalue σ almost remains unchanged with p, as shown in figure 10, because the dominant wavenumber $\mu + p$ with $0 \le p \le 1/2$ is nearly equal to μ . On the other hand, for small values of $|\mu|$, namely for small-wavenumber

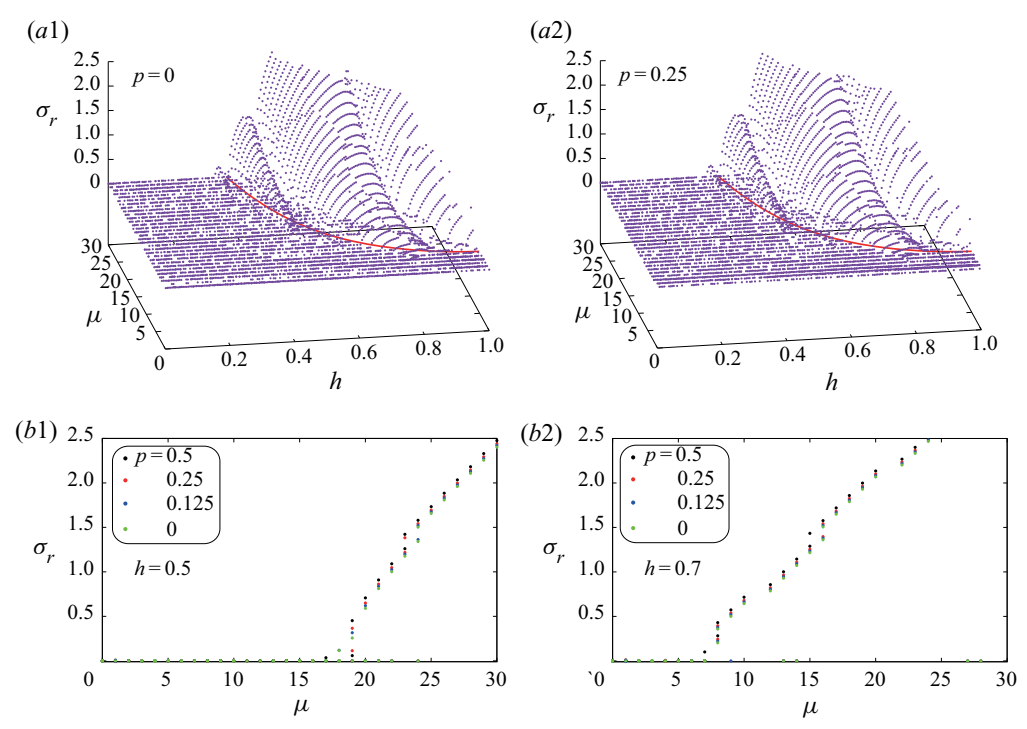


Figure 10. Variation of the growth rate σ_r with the wave steepness h and the dominant mode number μ for the density ratio $\rho_1/\rho_2=0.9$ and different values of the exponent p: (a) variation of σ_r with h and μ ; (b) variation of σ_r with μ . (a1) and (a2) show variation of σ_r with h and μ for p=0 and 0.25, respectively. (b1) and (b2) show variation of σ_r with μ for h=0.5 and 0.7, respectively. The results (dots) are computed with N=128 and M=60. The red solid line in (a) represents on the (μ , h)-plane the approximate critical mode number $\mu=\tilde{\mu}_c^{(KH)}(h)$ defined by (5.2).

(long-wavelength) disturbances, the eigenvalue σ changes with p and a different type of instability is observed, to be discussed in § 6.2.

6.2. Small-wavenumber instability

Until now, we have discussed the instability associated with large values of the dominant mode number μ , but the instability for which μ is small is also observed. Figure 11 shows the variation of the growth rate σ_r with the exponent p for $\mu=-1$, 1 and 0. Here, we fix the density ratio to $\rho_1/\rho_2=0.9$, but vary the wave steepness: (a) h=0.3, (b) 0.5, (c) 0.7 and (d) 0.9. The computed results using the present method are compared with (i) the approximate growth rate $\tilde{\sigma}_r^{(\text{NLS})}$ in (5.6) for the modulational instability and (ii) the computed results using the previous method (Yuen 1984) that was developed in the physical plane. It is found that the approximate growth rate $\tilde{\sigma}_r^{(\text{NLS})}$ is valid only for small values of h and p, as expected. It is also noticed that the computed results using the previous method agree with those using the present method only for $h \leq 0.7$, but not for h = 0.9. For h > 0.7, we could not obtain accurate numerical solutions using the previous method, as shown in figure 11(d).

It should be remarked that the value of the growth rate $\sigma_r > 0$ of small-wavenumber disturbances in figure 11 is much smaller than that of the wave-induced KH instability in § 6.1. Thus, it is difficult to identify the small-wavenumber instabilities with $\mu = -1$, 0 and 1, including the modulational instability in figures 7, 8, 9 and 10. It is interesting to

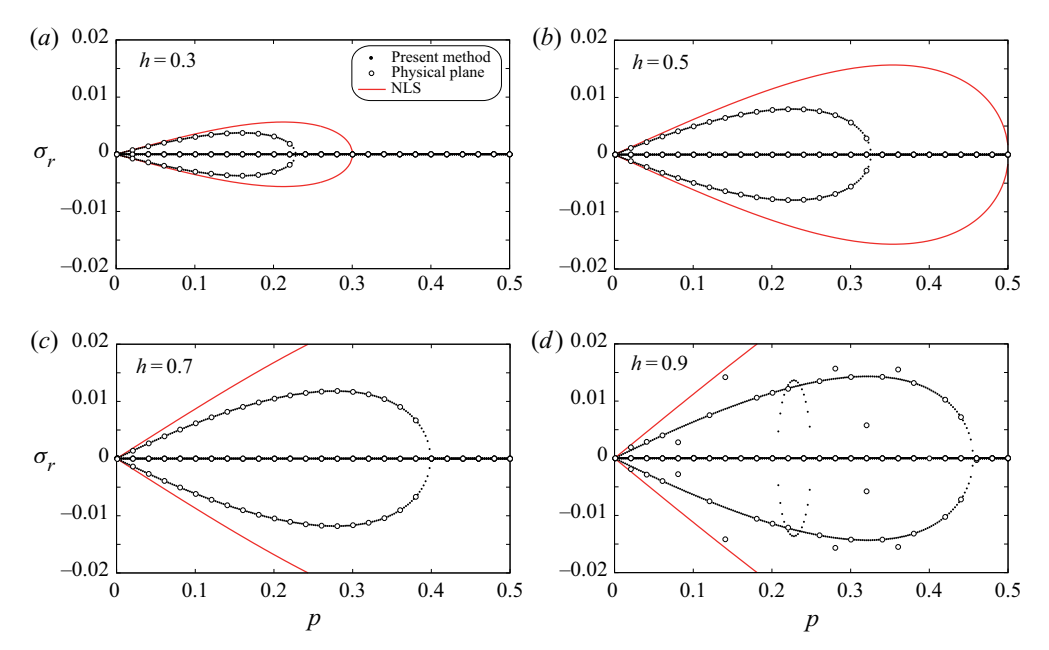


Figure 11. Variation of the growth rate σ_r with the exponent p for the density ratio $\rho_1/\rho_2 = 0.9$ and the dominant mode numbers $\mu = -1$, 0 and 1. The computed results using the present method with N = 128 and M = 60 (dots) are compared with those using the previous method by (Yuen 1984) (circles) and the approximate growth rate $\tilde{\sigma}_r^{(NLS)}$ in (5.6) for the modulational instability (red lines).

note that the present method captures another type of instability for h=0.9 and 0.21 , as shown in figure <math>11(d). This instability seems to be similar to the 'nonlinear mode jumping' phenomenon described by Yuen (1984, figure 4(g) on p. 80) for $\rho_1/\rho_2=0.9$ and h=0.5 with the background current jump $\Delta U=0.5(c_0/c)$. The source of this instability remains unknown and is a topic for future research.

7. Conclusions

We have performed linear stability analysis of finite-amplitude gravity waves at the interface between two unbounded homogeneous fluids of different density in the absence of background currents. We have focused on the wave-induced KH instability, which is excited by the tangential velocity jump at the interface induced by the deformation of the interface. To numerically study the linear stability for a wide range of wave steepnesses, the unsteady conformal mapping technique often adopted for surface waves is extended to the two-layer fluid problem, and the upper and lower flow domains are conformally mapped into the upper and lower half-planes, respectively. Then, the time-varying interface is always mapped onto the real axis and is conveniently parameterized. After reformulating the linear stability problem as the generalized eigenvalue problem in matrix form (4.32) in § 4.2, we numerically solved the eigenvalue problem (4.32), and have identified the dominant mode μ defined by (4.34) monitoring the eigenvectors of unstable disturbances.

The stability analysis in § 6.1 has confirmed that the wave-induced KH instability is the dominant mechanism for the instability of the interfacial periodic waves. This has been widely accepted, but has not been fully or accurately investigated in previous studies. Once the wave-induced KH instability is excited, large-wavenumber disturbances grow

exponentially if their wavenumbers are greater than a critical value that depends on the wave steepness and the density ratio. The critical mode number μ_c can be relatively well approximated by $\tilde{\mu}_c^{(KH)}$ in (5.2) for $\rho_1/\rho_2 \geqslant 0.3$, where $\tilde{\mu}_c^{(KH)}$ represents the critical value predicted by the local KH stability analysis by assuming that the local currents are constant around the wave crest, or, more specifically, over a length scale greater than the wavelengths of unstable waves. Nevertheless, the local stability analysis fails to accurately provide the growth rates, in particular, of large-wavenumber disturbances. In addition, it has been found that the successive collisions of the eigenvalues give rise to the wave-induced KH instability.

It has been shown in § 6.2 that small-wavenumber disturbances are also unstable and the present method allows us to numerically study such instability for large-amplitude waves, for which weakly nonlinear theory using the NLS equation is no longer applicable.

We have shown that the present method can be used to obtain accurate numerical solutions of the eigenvalue problem (4.32) for $\rho_1/\rho_2 \le 0.99$, $h \le 1$ and $|\mu| \le 40$ with N=128 and M=60, where N and M denote the total number of terms of the truncated Fourier series (A5) for steady wave solutions and (4.25) for the presentation of disturbances, respectively. Beyond this parameter range, the values of N and M need to be further increased with a more efficient numerical algorithm to solve the generalized eigenvalue problem.

Acknowledgement. The authors thank an anonymous reviewer for his/her detailed comments that have greatly improved the manuscript.

Funding. The work of S.M. was supported by JSPS KAKENHI grant no. JP17H02856 and the Research Institute for Mathematical Sciences, an International Joint Usage/Research Centre located in Kyoto University. The work of W.C. was supported by the US National Science Foundation through grant number DMS-2108524 and the Brain Pool Program funded by the Ministry of Science and ICT through the National Research Foundation of Korea (Grant No. 2021H1D3A2A01082312).

Declaration of interests. The authors report no conflict of interest.

Author ORCIDs.

- Sunao Murashige https://orcid.org/0000-0002-8393-9739;
- Wooyoung Choi https://orcid.org/0000-0002-4433-3013.

Appendix A. Numerical computation of steady interfacial waves

A.1. Numerical method

For steady wave solutions $z_j^{(0)}(\zeta_j)$ and $f_j^{(0)}(\zeta_j)$ in (3.1), the kinematic conditions (2.18) with (2.21*a*–*d*) yield

$$\tilde{\phi}_{j,j}^{(0)} = 1$$
 and $\tilde{\psi}_{j,j}^{(0)} = 0$ $(j = 1, 2),$ (A1)

and the dynamic condition (2.19) with (A1) becomes

$$G_1(\hat{\xi}) := \frac{1}{2} \frac{1}{J_2^{(0)}(\xi_2)} + \frac{1}{c^2} \tilde{y}_2^{(0)}(\xi_2) - \frac{\rho_1}{\rho_2} \left\{ \frac{1}{2} \frac{1}{J_1^{(0)}(\xi_1)} + \frac{1}{c^2} \tilde{y}_1^{(0)}(\xi_1) \right\} - \frac{B^{(0)}}{2} = 0, \quad (A2)$$

where $\xi_j = \hat{\xi}_j^{(0)}(\hat{\xi})$ (j = 1, 2) at the interface are given by (3.2), $J_j^{(0)}(\xi_j) = (\tilde{x}_{j,j}^{(0)})^2 + (\tilde{y}_{j,j}^{(0)})^2$ (j = 1, 2) and $B^{(0)}$ is an unknown real constant. The contact conditions (2.16) become

$$G_{2}(\hat{\xi}) := \tilde{x}_{1}^{(0)}(\xi_{1} = \hat{\xi} + \gamma^{(0)}(\hat{\xi})) - \tilde{x}_{2}^{(0)}(\xi_{2} = \hat{\xi} - \gamma^{(0)}(\hat{\xi})) = 0$$

$$G_{3}(\hat{\xi}) := \tilde{y}_{1}^{(0)}(\xi_{1} = \hat{\xi} + \gamma^{(0)}(\hat{\xi})) - \tilde{y}_{2}^{(0)}(\xi_{2} = \hat{\xi} - \gamma^{(0)}(\hat{\xi})) = 0$$
(A3)

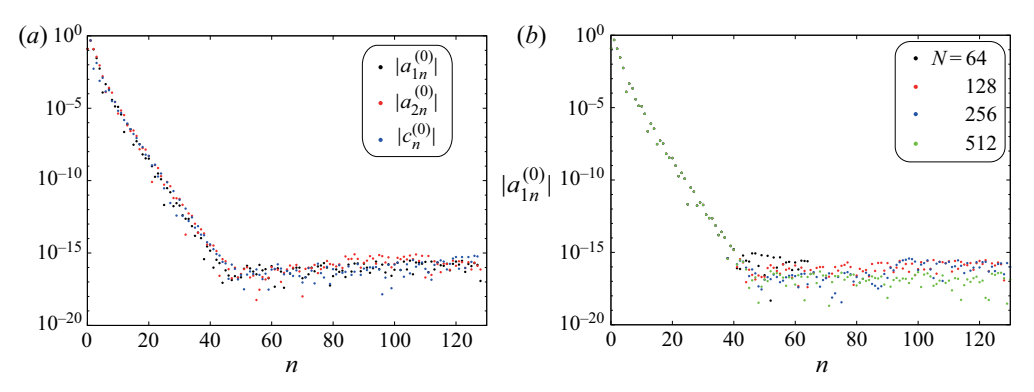


Figure 12. Fourier coefficients of steady wave solutions in (A4) for the density ratio $\rho_1/\rho_2=0.9$ and the wave steepness h=1.0: (a) $a_{1n}^{(0)}$, $a_{2n}^{(0)}$ and $c_n^{(0)}$ ($n=0,1,\ldots,N$) with N=128; (b) convergence of $a_{1n}^{(0)}$ with increasing N (N=64,128,256,512).

From the symmetry of the periodic wave profile, the analyticity of $z_j^{(0)} = x_j^{(0)} + \mathrm{i} y_j^{(0)}$ (j=1,2), the conditions at infinities (2.20) and the boundary conditions $\xi_j^{(0)}(\hat{\xi}=0)=0$, $\xi_j^{(0)}(\hat{\xi}=\pm\pi)=\pm\pi$ (j=1,2) and $\gamma^{(0)}(\hat{\xi}=0)=0$, $\gamma^{(0)}(\hat{\xi}=\pm\pi)=0$, we can expand the steady wave solutions $z_j^{(0)}(j=1,2)$ and $\gamma^{(0)}(j=1,2)$ as

$$z_{1}^{(0)}(\zeta_{1}) = \zeta_{1} + i \sum_{n=0}^{\infty} a_{1n}^{(0)} e^{in\zeta_{1}}$$

$$z_{2}^{(0)}(\zeta_{2}) = \zeta_{2} + i \sum_{n=0}^{\infty} a_{2n}^{(0)} e^{-in\zeta_{2}}$$
and
$$\gamma^{(0)}(\hat{\xi}) = \sum_{n=1}^{\infty} c_{n}^{(0)} \sin n\hat{\xi}, \quad (A4)$$

where $a_{1n}^{(0)}, a_{2n}^{(0)}, c_n^{(0)} \in \mathbb{R}$. For numerical calculations, each infinite series in (A4) is truncated as

$$\sum_{n=0}^{\infty} \sim \sum_{n=0}^{N}.$$
 (A5)

When the density ratio ρ_1/ρ_2 and the wave steepness h are given, we may numerically determine the 3N+3 unknowns $\{a_{1n}^{(0)}\}_{n=0}^N$, $\{a_{2n}^{(0)}\}_{n=0}^N$, $\{c_n^{(0)}\}_{n=1}^{N-1}$, B_0 and c using Newton's method such that the dynamic condition $G_1(\hat{\xi})=0$ in (A2) and the contact condition $G_3(\hat{\xi})=0$ in (A3) at $\hat{\xi}=\hat{\xi}_\ell=\ell\pi/N$ ($\ell=0,1,\ldots,N$), $G_2(\hat{\xi})=0$ in (A3) at $\hat{\xi}=\hat{\xi}_\ell$ ($\ell=1,2,\ldots,N-1$) with the wave height condition

$$G_4 := \tilde{y}_1^{(0)}(\xi_1 = 0) - \tilde{y}_1^{(0)}(\xi_1 = \pi) - h = 0, \tag{A6}$$

and the zero mean level condition

$$G_5 := \int_0^{\pi} \tilde{y}_1^{(0)} \tilde{x}_{1,1}^{(0)} \, \mathrm{d}\xi_1 = 0, \tag{A7}$$

are simultaneously satisfied. In the numerical results in this paper, the stopping condition of Newton's method was set to

$$\max\{\|G_1\|_{max}, \|G_2\|_{max}, \|G_3\|_{max}, |G_4|, |G_5|\} < 10^{-9}, \tag{A8}$$

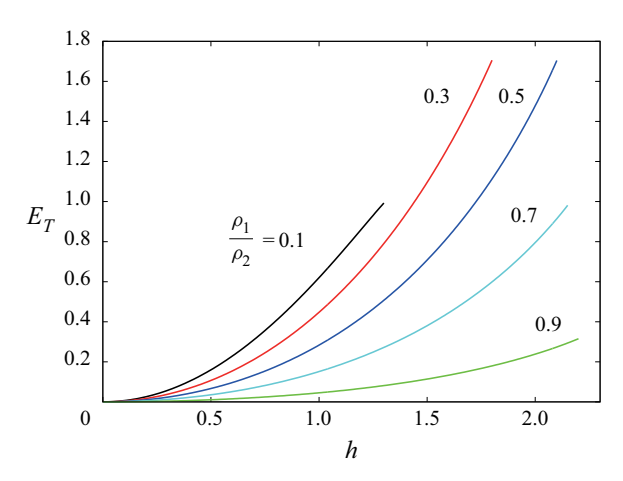


Figure 13. Variation of the total wave energy $E_T = E_K + E_P$ of steady interfacial waves with the wave steepness h for different values of the density ratio ρ_1/ρ_2 . The kinetic energy E_K and the potential energy E_P are computed by using (A9) and (A10), respectively, with the computed steady wave solutions with N = 128.

where

$$||G_j||_{max} = \max_{\ell=0,\dots,N} |G_j(\hat{\xi}_\ell)| \ (j=1,3) \ \text{and} \ ||G_2||_{max} = \max_{\ell=1,\dots,N-1} |G_2(\hat{\xi}_\ell)|.$$

Figure 12(a) shows the Fourier coefficients $a_{1n}^{(0)}$, $a_{2n}^{(0)}$ and $c_n^{(0)}$ in (A4) for $\rho_1/\rho_2=0.9$ and h=1.0. As they decay fast enough, any value of N greater than 60 seems to be large enough for double precision computations. In addition, as shown in figure 12(b), the Fourier coefficient $a_{1n}^{(0)}$ converges well as N increases. In this work, we use N=128.

In the linear stability analysis presented in § 4, to reduce numerical errors in solving eigenvalue problems, each Fourier coefficient in (A4) is set to zero if its absolute value is less than 10^{-13} .

A.2. Wave energy

The expressions for the kinetic energy E_K and the potential energy E_P of steady interfacial waves of symmetric profile are given by

$$E_K = \frac{1}{2}c^2 \left[\frac{\rho_1}{\rho_1 + \rho_2} \iint_{\mathcal{D}_1} \{ (u_1 - 1)^2 + v_1^2 \} \, d\tilde{x} \, d\tilde{y} + \frac{\rho_2}{\rho_1 + \rho_2} \iint_{\mathcal{D}_2} \{ (u_2 - 1)^2 + v_2^2 \} \, d\tilde{x} \, d\tilde{y} \right]$$

$$= c^2 \left[\int_0^{\pi} y_1^{(0)} \gamma_{\hat{\xi}}^{(0)} \, d\hat{\xi} - \left(\frac{1 - \rho_1/\rho_2}{1 + \rho_1/\rho_2} \right) \int_0^{\pi} y_1^{(0)} \{ 1 - x_{1,1}^{(0)} (1 + \gamma_{\hat{\xi}}^{(0)}) \} \, d\hat{\xi} \right], \tag{A9}$$

and

$$E_{P} = -\frac{\rho_{1}}{\rho_{1} + \rho_{2}} \int_{x_{A}}^{x_{B}} \int_{0}^{\tilde{y}} y \, dy \, dx + \frac{\rho_{2}}{\rho_{1} + \rho_{2}} \int_{x_{A}}^{x_{B}} \int_{0}^{\tilde{y}} y \, dy \, dx$$

$$= \left(\frac{1 - \rho_{1}/\rho_{2}}{1 + \rho_{1}/\rho_{2}}\right) \int_{0}^{\pi} \{y_{1}^{(0)}\}^{2} x_{1,1}^{(0)} (1 + \gamma_{\hat{\xi}}^{(0)}) \, d\hat{\xi}, \tag{A10}$$

where each energy is non-dimensionalized by $(\rho_1 + \rho_2)g/k^3$, and \mathcal{D}_j (j = 1, 2) denote the fluid domains surrounded by A_jACBB_j in figure 1(a). Figure 13 shows the variation of the total wave energy $E_T = E_K + E_P$ of steady interfacial waves with the wave steepness h.

It was shown by Tanaka (1983) and Longuet-Higgins & Tanaka (1997) that the steady surface gravity waves lose stability due to superharmonic disturbances at the wave amplitude where the wave energy attains an extremum. Murashige & Choi (2020) also found that this type of superharmonic instability of surface waves occurs even in the presence of a linear shear current. In this work, we compute steady solutions only for $h \leq 1$, where the wave energy E_T increases monotonically with h. Thus the superharmonic instability found for surface waves does not occur for the interfacial waves with $h \leq 1$.

Appendix B. The coefficient functions $A_{*,m}(\hat{\xi})$, $B_{*,m}(\hat{\xi})$ and $C_{*,m}(\hat{\xi})$

The coefficient functions $A_{*,m}(\hat{\xi})$, $B_{*,m}(\hat{\xi})$ and $C_{*,m}(\hat{\xi})$ in (4.15), (4.16), (4.17) and (4.18*a*,*b*) are given by

$$A_{11,m}(\hat{\xi}) = \left\{ \tilde{x}_{1,1}^{(0)} - i \operatorname{sgn}(p+m) \, \tilde{y}_{1,1}^{(0)} \right\} \exp(i(p+m)\gamma^{(0)}(\hat{\xi})) \exp(im\hat{\xi})$$

$$B_{11,m}(\hat{\xi}) = -|p+m| \exp(i(p+m)\gamma^{(0)}(\hat{\xi})) \exp(im\hat{\xi})$$

$$A_{21,m}(\hat{\xi}) = \frac{\rho_1}{\rho_2} \frac{1}{J_1^{(0)}} \left\{ i \operatorname{sgn}(p+m) \, \tilde{x}_{1,1}^{(0)} + \tilde{y}_{1,1}^{(0)} \right\} \exp(i(p+m)\gamma^{(0)}(\hat{\xi})) \exp(im\hat{\xi})$$

$$A_{22,m}(\hat{\xi}) = -\frac{1}{J_2^{(0)}} \left\{ -i \operatorname{sgn}(p+m) \, \tilde{x}_{2,2}^{(0)} + \tilde{y}_{2,2}^{(0)} \right\} \exp(-i(p+m)\gamma^{(0)}(\hat{\xi})) \exp(im\hat{\xi})$$

$$B_{21,m}(\hat{\xi}) = -\frac{\rho_1}{\rho_2} \exp(i(p+m)\gamma^{(0)}(\hat{\xi})) \exp(im\hat{\xi}),$$

$$B_{22,m}(\hat{\xi}) = \exp(-i(p+m)\gamma^{(0)}(\hat{\xi})) \exp(im\hat{\xi})$$

$$B_{22,m}(\hat{\xi}) = \exp(-i(p+m)\gamma^{(0)}(\hat{\xi})) \exp(im\hat{\xi})$$
(B2)

$$A_{31,m}(\hat{\xi}) = \frac{\rho_1}{\rho_2} \left[-\frac{1}{(J_1^{(0)})^2} \left\{ i \operatorname{sgn}(p+m) \tilde{x}_{1,1}^{(0)} + \tilde{y}_{1,1}^{(0)} \right\} i(p+m) + \frac{1}{c^2} \right] \\
\times \exp(i(p+m)\gamma^{(0)}(\hat{\xi})) \exp(im\hat{\xi}) \\
A_{32,m}(\hat{\xi}) = \left[\frac{1}{(J_2^{(0)})^2} \left\{ -i \operatorname{sgn}(p+m) \tilde{x}_{2,2}^{(0)} + \tilde{y}_{2,2}^{(0)} \right\} i(p+m) - \frac{1}{c^2} \right] \\
\times \exp(-i(p+m)\gamma^{(0)}(\hat{\xi})) \exp(im\hat{\xi}) \\
B_{31,m}(\hat{\xi}) = \frac{\rho_1}{\rho_2} \frac{1}{J_1^{(0)}} i(p+m) \exp(i(p+m)\gamma^{(0)}(\hat{\xi})) \exp(im\hat{\xi}) \\
B_{32,m}(\hat{\xi}) = -\frac{1}{J_2^{(0)}} i(p+m) \exp(-i(p+m)\gamma^{(0)}(\hat{\xi})) \exp(im\hat{\xi}) \\
C_{3,m}(\hat{\xi}) = \left[-\frac{\frac{1}{2}J_{2,2}^{(0)}}{(J_2^{(0)})^2} + \frac{1}{c^2} \tilde{y}_{2,2}^{(0)} + \frac{\rho_1}{\rho_2} \left\{ -\frac{\frac{1}{2}J_{1,1}^{(0)}}{(J_1^{(0)})^2} + \frac{1}{c^2} \tilde{y}_{1,1}^{(0)} \right\} \right] \exp(im\hat{\xi}) \\
A_{41,m}(\hat{\xi}) = \operatorname{sgn}(p+m) \exp(i(p+m)\gamma^{(0)}(\hat{\xi})) \exp(im\hat{\xi}) \\$$

 $A_{42,m}(\hat{\xi}) = \operatorname{sgn}(p+m) \exp(-\mathrm{i}(p+m)\gamma^{(0)}(\hat{\xi})) \exp(\mathrm{i}m\hat{\xi})$

 $C_{4,m}(\hat{\xi}) = i (\tilde{x}_{1,1}^{(0)} + \tilde{x}_{2,2}^{(0)}) \exp(im\hat{\xi})$

(B4)

$$A_{51,m}(\hat{\xi}) = \left\{ \tilde{x}_{1,1}^{(0)} + \tilde{x}_{2,2}^{(0)} - i \operatorname{sgn}(p+m)(\tilde{y}_{1,1}^{(0)} + \tilde{y}_{2,2}^{(0)}) \right\} \times \exp(i(p+m)\gamma^{(0)}(\hat{\xi})) \exp(im\hat{\xi})$$

$$A_{52,m}(\hat{\xi}) = \left\{ \tilde{x}_{1,1}^{(0)} + \tilde{x}_{2,2}^{(0)} + i \operatorname{sgn}(p+m)(\tilde{y}_{1,1}^{(0)} + \tilde{y}_{2,2}^{(0)}) \right\} \times \exp(-i(p+m)\gamma^{(0)}(\hat{\xi})) \exp(im\hat{\xi})$$

$$\times \exp(-i(p+m)\gamma^{(0)}(\hat{\xi})) \exp(im\hat{\xi})$$

$$B_{51,m}(\hat{\xi}) = A_{41,m}(\hat{\xi}) \quad \text{and} \quad B_{52,m}(\hat{\xi}) = -A_{42,m}(\hat{\xi})$$
(B5)

REFERENCES

BAKER, G.R., MEIRON, D.I. & ORSZAG, S.A. 1982 Generalized vortex methods for free-surface flow problems. *J. Fluid Mech.* 123, 477–501.

BENJAMIN, T.B. & BRIDGES, T.J. 1997 Reappraisal of the Kelvin–Helmholtz problem. Part 2. Interaction of the Kelvin–Helmholtz, superharmonic and Benjamin–Feir instabilities. *J. Fluid Mech.* 333, 327–373.

CHOI, W. & CAMASSA, R. 1999 Exact evolution equations for surface waves. J. Engng Mech. ASCE 125, 756–760.

DIXON, A. 1990 A stability analysis for interfacial waves using Zakharov equation. *J. Fluid Mech.* 214, 185–210.

DYACHENKO, A.L., ZAKHAROV, V.E. & KUZNETSOV, E.A. 1996 Analytical description of the free surface dynamics of an ideal fluid (canonical formalism and conformal mapping). *Phys. Lett.* A **221**, 73–79.

DRAZIN, P.G. & REID, W.H. 1981 Hydrodynamic Stability. Dover.

GRIMSHAW, R.H.J. & PULLIN, D.I. 1985 Stability of finite-amplitude interfacial waves. Part 1. Modulational instability for small-amplitude waves. J. Fluid Mech. 160, 297–315.

GRUE, J., FRIIS, A., PALM, E. & RUSÅS, P.O. 1997 A method for computing unsteady fully nonlinear interfacial waves. J. Fluid Mech. 351, 223–252.

HOLYER, J.Y. 1979 Large amplitude progressive interfacial waves. J. Fluid Mech. 93, 433-448.

LAMB, H. 1945 Hydrodynamics, 6th edn. Dover.

LONGUET-HIGGINS, M.S. & TANAKA, M. 1997 On the crest instabilities of steep surface waves. *J. Fluid Mech.* 336, 51–68.

MACKAY, R.S. & SAFFMAN, P.G. 1986 Stability of water waves. Proc. R. Soc. Lond. A 406, 115-125.

MCLEAN, J.W. 1982 Instabilities of finite-amplitude water waves. J. Fluid Mech. 114, 315–330.

MEI, C.C., STIASSNIE, M. & YUE, D.K.P. 2005 Theory and Applications of Ocean Surface Waves, Part 2: Nonlinear Aspects. World Scientific.

MEIRON, D.I. & SAFFMAN, P.G. 1983 Overhanging interfacial gravity waves of large amplitude. *J. Fluid Mech.* 129, 213–218.

MURASHIGE, S. & CHOI, W. 2020 Stability analysis of deep-water waves on a linear shear current using unsteady conformal mapping. *J. Fluid Mech.* 885, A41.

OVSHANNIKOV, L. 1974 To the shallow water theory foundation. Arch. Mech. 26, 407–422.

PĂRĂU, E. & DIAS, F. 2001 Interfacial periodic waves of permanent form with free-surface boundary conditions. J. Fluid Mech. 437, 325–336.

PULLIN, D.I. & GRIMSHAW, R.H.J. 1985 Stability of finite-amplitude interfacial waves. Part 2. Numerical results. *J. Fluid Mech.* **160**, 317–336.

SAFFMAN, P.G. & YUEN, H.C. 1982 Finite-amplitude interfacial waves in the presence of a current. *J. Fluid Mech.* 123, 459–476.

TANAKA, M. 1983 The stability of steep gravity waves. J. Phys. Soc. Japan 52, 3047–3055.

TANVEER, S. 1991 Singularities in water waves and Rayleigh–Taylor instability. *Proc. R. Soc. Lond.* A 435, 137–158.

TIRON, R. & CHOI, W. 2012 Linear stability of finite-amplitude capillary waves on water of infinite depth. *J. Fluid Mech.* **696**, 402–422.

TSUJI, Y. & NAGATA, Y. 1973 Stokes' expansion of internal deep water waves to the fifth order. *J. Oceanogr. Soc. Japan* 29, 61–69.

TURNER, R.E.L. & VANDEN-BROECK, J.-M. 1986 The limiting configuration of interfacial gravity waves. *Phys. Fluids* **29**, 372–375.

- VANDEN-BROECK, amplitude. Phys. Fluids 23, 1723–1726. 1980 Numerical calculation of gravity-capillary interfacial waves of finite
- YUEN, H. 1984 Nonlinear dynamics of interfacial waves. *Physica* D 12, 71–82. ZHOU, C.P., LEE, J.H.W. & CHEUNG, Y.K. 1992 Instabilities and bifurcations of interfacial water waves. *Phys. Fluids* A 4, 1428–1438.